Interaction Notes

Note 402

November 1980

SEM CHARACTERIZATION OF THE ELECTROMAGNETIC SCATTERING FROM THIN AND THICK OPEN-ENDED CYLINDERS

Gary Bruce Melson
L. Wilson Pearson
University of Kentucky
Lexington, Kentucky 40506

ABSTRACT

The results of a numerical study to determine the SEM parameters which characterize the transient and time-harmonic electromagnetic scattering from an open-ended conducting cylinder are presented and discussed. This structure provides an interesting object in terms of which physical significance of various SEM pole constituents may be interpreted. Limiting cases -- fat and thin -- of the structure are strongly akin to, respectively, the wire loop and the thin wire scatterer so that pole location and the features of the associated modes can be tracked from one limit to the other. One conclusion drawn from this work is the likely validation of the conjecture due to Wilton connecting the so-called type III poles for the wire loop to interior resonances for closed bodies. Further conclusions are drawn relative to features of the poles associated with higher-order azimuthal variation. The exterior modes associated with these higher-order variations exhibit substantially higher damping than those of zeroth-order azimuthal variation. This damping can be associated with radiation due to torsional flow paths of the higher-order current modes. Results of the SEM calculations supporting these and other conclusions are presented.

This work was sponsored, in part, by the Rome Air Development Center Postdoctoral Program and, in part, by the New Mexico State University Physical Sciences Laboratory under Contract Number 284. Computing facilities on the CRAY-1 computer were provided by the Air Force Weapons Laboratory, Kirtland AFB NM.

ACKNOWLEDGEMENTS

The encouragement of Mr. Jay L. Wilson of New Mexico State University's Physical Sciences Laboratory toward applying SEM in the present context is acknowledged. The authors are sincerely grateful to Mr. Krzysztof A. Michalski for many generous hours of assistance spent in the formulation of the computer algorithm and for his unyielding support during the completion of this project. Sincere gratitude is extended to Mr. John Roberts for his assistance in the computation of the data base contained herein. We also thank Ms. Gail McAlister for her able assistance in the typing of the equations and Mr. Joey Grasty for the drafting of the figures and plotting of the three-dimensional graphs contained in this work.

TABLE OF CONTENTS

LIST OF FIGURES

CHAPTER 1

INTRODUCTION

This work considers the Singularity Expansion Method (SEM) characterization of the electromagnetic scattering by a thin-walled open-ended cylinder. The cylindrical structure considered can range from very thin, such as conventional "thin-wire" theories might treat, to moderately thick with length to diameter ratios approaching unity. The data determined through the work reported here are ultimately to be applied in estimating the resonant frequencies of the induced surface current on the object for time-harmonic excitations.

The Singularity Expansion Method was introduced by Baum in 1971 [1]. It was originally postulated for the prediction of transient scattering responses, however, it now appears to have equal utility in frequency-domain applications. While a great deal of activity has proceeded in applying SEM to transient problems (c.f. the reviews of [2] and [3]), less effort has been directed toward time-harmonic applications. Tesche used the SEM representation for current on a thin wire to determine the frequency-dependent admittance of a center-driven wire

[4]. More recently, Pearson has suggested further frequency domain applications [5] and, in work related to that reported here, has described the use of SEM in the interpretation of the frequency-dependent coupling of electromagnetic energy to shielding shells -- in particular cylindrical and cylinder-like structures -- in the context of electromagnetic interference [6]. SEM is particularly useful in this context because it allows an all-embracing characterization of the scatterer response over both a broad frequency range and over all spatial forms of the excitation: for example a plane wave with an arbitrary direction of arrival, a spherical wave, etc.

The thick open-ended cylinder is an important object for study because it is the canonical shape for a wide variety of missile structures. The shape of appropriate cylinder models for such structures can range from moderately thin to moderately thick -- sufficiently thick that the azimuthal variation of the current is significant. The computational model used in this work takes the azimuthal dependence of the current into account by way of the body of revolution approach used previously by Mautz and Harrington [7] and Glisson and Wilton [8] in more general contexts. We have used the electric field integral equation characterization of the scatterer and a method of moments procedure in which the electrostatic effects are given in terms of explicitly-stated surface charge density on the structure after Glisson and Wilton [8].

The SEM description for various thicknesses of cylinders are presented herein. A collection of the dominant resonances for the SEM description of currents induced on an open-ended cylindrical structure is reported for cylinder aspect ratios ranging from length/diameter of 100 to length/diameter of 3.333 for the zeroth-order azimuthal variation and the first-order azimuthal variation cases, and a partial collection of resonances for the second-order azimuthal variation case. The second-order case is included principally to show the degree of dominance of the zeroth and first order cases in the representation. The SEM parameters for a given scatterer include the complex resonances along with the associated modal current distributions and corresponding normalization constants. The poles are presented here for the twelve dominant resonances (those nearest the $j\omega$ axis) of the cylinder for specific aspect ratios 100, 50, 20, 10, 5, and 3.33 for the zeroth-order variation. For the first-order azimuthal variation case the twelve counterpart resonances are presented along with the first few resonances which correspond to waveguide modes on the side of the cylinder wall. The data presented for the second-order variation were selected to provide some perspective for the higher order azimuthal variations. Six "first-layer" resonances are presented for aspect ratios of 50, 10, and 3.33 for the second order azimuthal variation. Trajectories of pole movement with respect to variation of aspect ratio and the

interpretations of the natural modes are discussed. A complete tabulation of these data is given in a companion report [9].

This document reports a method of determination of the Singularity Expansion Method parameters for an open-ended cylinder. Chapter 2 presents the electric field integro-differential equation formulation along with the Method of Moment (MOM) [8] expansion which was used to solve it. The validation of this numerical method is discussed there. Selected results and their physical interpretation are presented in Chapter 3. Chapter 4 presents conclusions drawn from the present study and suggests new directions toward which it may be extended.

CHAPTER 2

DESCRIPTION OF FORMULATION

2.1 Introduction

An electric field integro-differential equation was used to characterize the cylinder and was solved using a method of moments technique. The solution to the electric field integral equation for a perfectly conducting open-ended cylindrical structure was obtained using a method of moments formulation with subsectional expansion - collocational testing procedures. The body of revolution approach was used to reduce the two-dimensional character of the problem to a one-dimensional one for various order harmonic current variations around the cylinder. The current and charge on the cylinder were expanded in unit pulses and the integral equation was tested with dirac-delta functions. Symmetry was exploited to reduce the number of unknowns and thereby improve the efficiency of the program for the extraction of the SEM parameters.

2.2 Formulation of the Integral Equation

The following formulation follows directly from the Body of Revolution approach of Glisson and Wilton [8] where their general body is specialized to a cylinder.

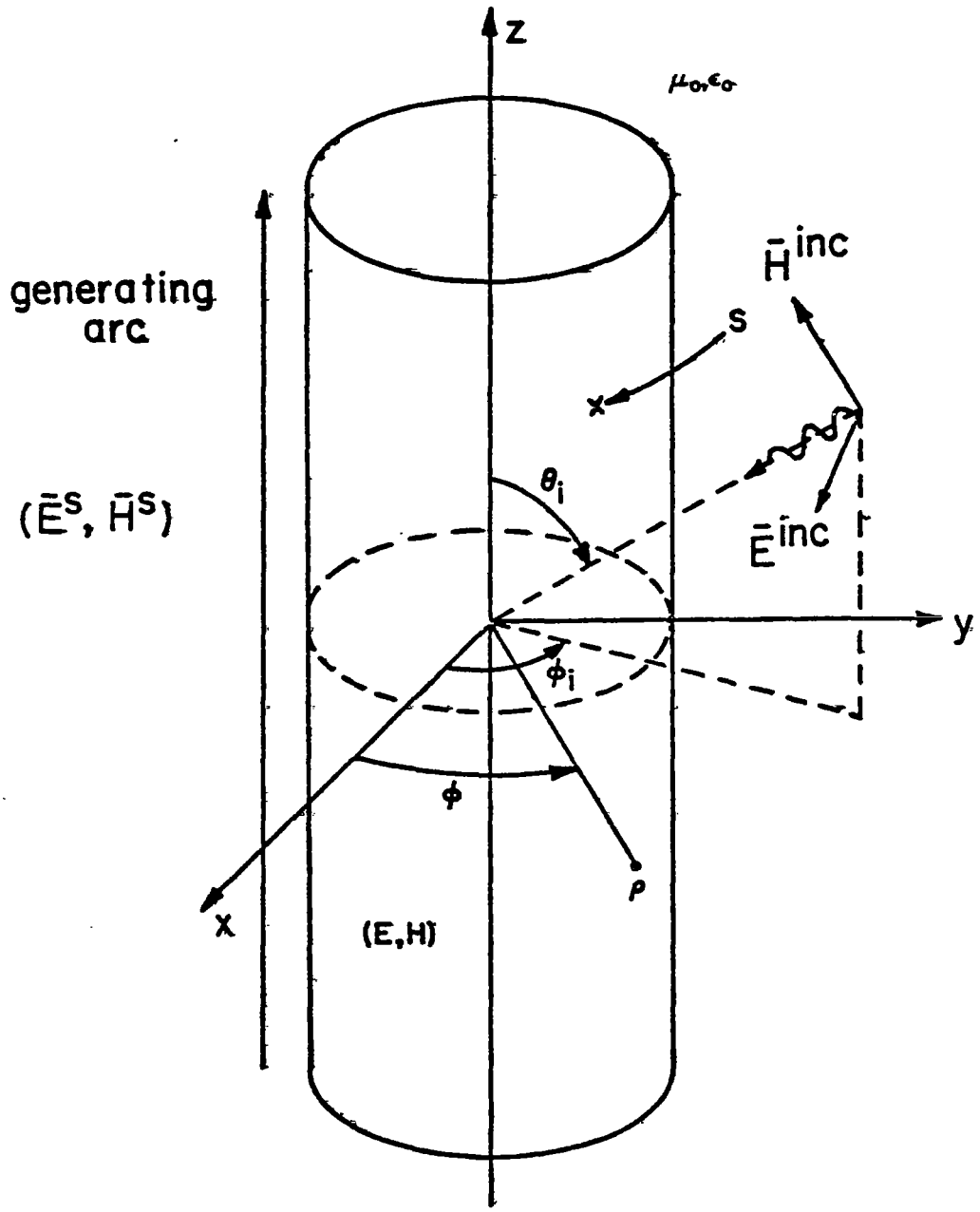

Figure 1. Geometry of the cylinder.

Consider the cylinder formed by rotating a planar curve - "generating arc" - around the z-axis (the axis of rotation) as shown in Figure 1, where S is defined as the surface of the cylindrical body. The perfectly conducting body is immersed in an infinite-extent homogeneous medium, with constituitive parameters (μ_o, ε_o).

Boundary conditions dictate that the total fields tangential to the surface of the body must vanish such that

$$-(\hat{n} \times \bar{E}^s) = \hat{n} \times \bar{E}^{inc}, \qquad (2.1)$$

where $\bar{E}^s$ is the scattered electric field, $\bar{E}^{inc}$ is the incident electric field, and $\bar{E} = \bar{E}^s + \bar{E}^{inc}$ is the total electric field present, and $\hat{n} = \hat{\phi} \times \hat{z}$ is the outward normal to the cylinder surface. Using the equivalence principle, the body can be replaced by a current $\bar{J}$ flowing in free space along the original contour of the cylinder's surface. This equivalent current represents the sum of the currents flowing on the interior and exterior walls of the cylindrical shell in the original problem.

The scattered electric field may be expressed as

$$\bar{E}^s(\bar{r}) = -s\bar{A}(\bar{r}) - \nabla\Phi(\bar{r}) \qquad (2.2)$$

---

* The formulation of eq.(2.2) through (2.6), where the frequency variable $s = \sigma + j\omega$ has been introduced, follows directly from the Laplace transform of the time dependent form of Maxwell's equations.

where the potentials are defined as

$$\bar{A}(\bar{r}) = (\mu/4\pi) \iint_S \bar{J}(\bar{r}')G(\bar{r},\bar{r}')\, dS' \quad , \tag{2.3a}$$

as

$$\phi(\bar{r}) = (1/4\pi\varepsilon) \iint_S \rho_s(\bar{r})G(\bar{r},\bar{r}')\, dS' \tag{2.3b}$$

with

$$G(\bar{r},\bar{r}') = \exp(-sR/c)/R \tag{2.4a}$$

and

$$R = |\bar{r} - \bar{r}'| = [\rho^2 + \rho'^2 - 2\rho\rho'\cos(\phi - \phi') + (z - z')^2]^{\frac{1}{2}} . \tag{2.4b}$$

The charge relates to the current through the continuity equation

$$\rho_s(\bar{r}) = -\mathrm{div}_s\, \bar{J}(\bar{r})/s = -\nabla_s \cdot \bar{J}(\bar{r})/s \quad . \tag{2.5}$$

Combining (2.1) through (2.5), allows one to express the electric field integral equation as

$$\hat{n} \times \bar{E}^{inc} = \hat{n} \times \{(s\mu/4\pi) \iint_S \bar{J}(\bar{r}')G(\bar{r},\bar{r}')\, dS'$$

$$- (1/4\pi s\varepsilon)\nabla \iint_S \nabla'_s \cdot \bar{J}(\bar{r}')G(\bar{r},\bar{r}')\, dS'\} . \tag{2.6}$$

Equation (2.6) can be written in operator form as

$$E_z^{inc}(z) = \beta_{11}(J_z) + \beta_{12}(J_\phi) \qquad (2.7a)$$

$$E_\phi^{inc}(z) = \beta_{21}(J_z) + \beta_{22}(J_\phi) \qquad (2.7b)$$

where β_{ij} are the integro-differential operators relating respective current and field components as identified from (2.6). To explicitly express these operators the need arises for the following transformations, in order to express source point coordinate bases in observation point coordinate bases:

$$\hat{a}_\rho' = \cos(\phi-\phi')\hat{a}_\rho - \sin(\phi-\phi')\hat{a}_\phi \ ; \qquad (2.8a)$$

$$\hat{a}_\phi' = \sin(\phi-\phi')\hat{a}_\rho + \cos(\phi-\phi')\hat{a}_\phi \ ; \text{ and} \qquad (2.8b)$$

$$\hat{a}_z' = \hat{a}_z \ . \qquad (2.8c)$$

Expanding the surface divergence in cylindrical coordinates and specializing it to the surface yields

$$\nabla_s' \cdot \bar{J} = (1/\rho)\partial/\partial\phi'(J_\phi) + \partial/\partial z'(J_z) \qquad (2.9)$$

Expanding the current in (2.6) into observation point unit

vector components, we obtain

$$\bar{J}(\bar{r}') = J_\phi(\bar{r}')\cos(\phi - \phi')\hat{a}_\phi + J_z(\bar{r}')\hat{a}_z \ . \qquad (2.10)$$

Using (2.8) and (2.9), and comparing with (2.7), the expressions for β_{ij} are identified to be

$$\beta_{11}(J_z) = \frac{s\mu}{4\pi}\iint_S J_z(\bar{r}')G(\bar{r},\bar{r}')\,ds'$$

$$- \frac{1}{4\pi s\varepsilon}\frac{\partial}{\partial z}\iint_S \frac{\partial}{\partial z'}J_z(\bar{r}')\,G(\bar{r},\bar{r}')\,ds' \ , \qquad (2.11a)$$

$$\beta_{12}(J_\phi) = -\frac{1}{4\pi s\varepsilon a}\frac{\partial}{\partial z}\iint_S \frac{\partial}{\partial \phi'}J_\phi(\bar{r}')\,G(\bar{r},\bar{r}')\,ds' \ , \qquad (2.11b)$$

$$\beta_{21}(J_z) = -\frac{1}{4\pi s\varepsilon a}\frac{\partial}{\partial \phi}\iint_S \frac{\partial}{\partial z'}J_z(\bar{r}')\,G(\bar{r},\bar{r}')\,ds' \ , \text{ and} \qquad (2.11c)$$

$$\beta_{22}(J_\phi) = \frac{s\mu}{4\pi}\iint_S J_\phi(\bar{r}')G(\bar{r},\bar{r}')\cos(\phi - \phi')\,ds'$$

$$- \frac{I}{4\pi s\varepsilon a^2}\frac{\partial}{\partial \phi}\iint_S \frac{\partial}{\partial \phi'}J_\phi(\bar{r}')\,G(\bar{r},\bar{r}')\,ds' \ . \qquad (2.11d)$$

For subsequent interpretive purposes, equation (2.6) can be written in the following dyadic operator form

$$\langle \bar{\bar{\Gamma}}(\bar{r},\bar{r}',s), \bar{J}(\bar{r}')\rangle = \tan\{\bar{E}^{inc}(\bar{r},s)\}, \quad \bar{r}\in S \qquad (2.12)$$

where the symmetric product is defined as

$$\langle \bar{F};\bar{G} \rangle = \iint_S \bar{F}\cdot\bar{G}\, dS \ . \tag{2.13}$$

The operator statement of the integral equation of (2.12) constitutes a complete electromagnetic description of the given scatter. As a consequence the operator $\bar{\bar{\Gamma}}$ has associated with it all of the SEM poles for the structure. Because the structure is rotationally-symmetric, we may apply the body of revolution approach [7,8] to decompose the all-encompassing form (2.12) into a collection of integral equations, which are similar in form, associated with harmonic variation orders m=0, 1, 2, ... This procedure provides a natural subdivision of the SEM data into sets associated with the various harmonic orders. The harmonic decomposition of (2.12) proceeds from expanding the current in (2.10) in a Fourier series

$$\bar{J}(a,\phi',z') = \frac{I}{2\pi} \sum_{n=-\infty}^{\infty} J_{\phi n}(z')\cos(\phi-\phi')e^{jn\phi'}\,\hat{a}_\phi + \frac{I}{2\pi} \sum_{n=-\infty}^{\infty} J_{zn}(z')e^{jn\phi'}\,\hat{a}_z \ . \tag{2.14}$$

The incident electric field along with the kernel term are also expanded into their corresponding Fourier series,

$$\bar{E}^{inc}(a,\phi,z) = \frac{I}{2\pi} \sum_{m=-\infty}^{\infty} E^{inc}_{\phi m}(z)e^{jm\phi}\,\hat{a}_\phi + \frac{I}{2\pi} \sum_{m=-\infty}^{\infty} E^{inc}_{zm}(z)e^{jm\phi}\,\hat{a}_z \tag{2.15}$$

and

$$G(\bar{r},\bar{r}') = \exp(-sR/c)/R = \frac{1}{2\pi}\sum_{m=-\infty}^{\infty} G_m(z,z')e^{jm(\phi-\phi')} \quad (2.16)$$

where observing the evenness of the kernel with respect to $(\phi-\phi')$, and using Euler's identity, we obtain

$$G_m(z,z') = \int_{-\pi}^{\pi} (\exp(-sR/c)/R)\cos(m(\phi-\phi'))\, d(\phi-\phi') \,. \quad (2.17)$$

Substituting these back in (2.11), and accounting for the orthogonality of $e^{jm\phi}$, then (2.7) decomposes to the harmonic-by-harmonic coupled operator equations

$$E^{inc}_{zm}(z) = \beta_{11m}(J_{zm}) + \beta_{12m}(J_{\phi m}) \quad (2.18a)$$

$$E^{inc}_{\phi m}(z) = \beta_{21m}(J_{zm}) + \beta_{22m}(J_{\phi m}) \,. \quad (2.18b)$$

The operators for the respective harmonics are

$$\beta_{11m}(J_{zm}) = \frac{s\mu a}{4\pi}\int_{-h}^{h} J_{zm}(z')G_m(z,z')\, dz'$$

$$-\frac{a}{4\pi s\epsilon}\frac{\partial}{\partial z}\int_{-h}^{h}\frac{\partial}{\partial z'}J_{zm}(z')\, G_m(z,z')\, dz' \,, \quad (2.19a)$$

$$\beta_{12m}(J_{\phi m}) = -\frac{jm}{4\pi s\epsilon}\frac{\partial}{\partial z}\int_{-h}^{h} J_{\phi m}(z')G_m(z,z')\, dz' \,, \quad (2.19b)$$

$$\beta_{21m}(J_{zm}) = -\frac{1}{4\pi s\varepsilon}\frac{\partial}{\partial\phi}\int_{-h}^{h}\frac{\partial}{\partial z'}J_{zm}(z')\,G_m(z,z')\,dz' \quad , \text{ and} \qquad (2.19c)$$

$$\beta_{22m}(J_{\phi m}) = \frac{s\mu c}{4\pi}\int_{-h}^{h}J_{\phi m}(z')[G_{m+1}(z,z') + G_{m-1}(z,z')]\,dz'$$

$$-\frac{jm}{4\pi s\varepsilon a}\frac{\partial}{\partial\phi}\int_{-h}^{h}J_{\phi m}(z')G_m(z,z')\,dz' \quad . \qquad (2.19d)$$

2.3 SEM Characterization

In a fashion similar to the expression of (2.7) in the form given in (2.12), eq.(2.18) can be expressed on a harmonic-by-harmonic basis by

$$\langle\bar{\bar{\Gamma}}_m(\bar{r},\bar{r}',s);\bar{J}_m(\bar{r},s)\rangle = \tan\{\bar{E}_m^{inc}(\bar{r},s)\} \qquad (2.20)$$

Eq.(2.20) illustrates the total decoupling of each Fourier harmonic mode, and allows the determination of each harmonic current mode independently. This fact is of major importance in the determination of the SEM parameters. To be able to totally characterize the scatterer in it's SEM parameters, each mode can be solved separately and independently. Since the total current is the infinite summation of all of the modal currents then the total SEM parameters can now be found.

The SEM representation for the surface current on the cylinder proceeds from (2.12) and (2.20) as follows. The integral equations (2.20) possess homogeneous solutions

for a collection of complex frequencies (s_{mi}) for which $\bar{\bar{\Gamma}}$ is singular -- the complex natural resonances, or poles, associated with the m^{th} harmonic. Viz.

$$<\bar{\bar{\Gamma}}_m(\bar{r},\bar{r}',s_{mi});\bar{J}_{mi}(\bar{r})> = 0. \qquad (2.21)$$

The associated homogeneous solutions $\bar{J}_{mi}(\bar{r})$ to (2.21) are termed the natural modes. It is clear that the modes and poles are associated through the indices mi. The determination and physical interpretation of these quantities is the primary end of the work reported here. The numerical procedure applied to (2.20) for this purpose is discussed subsequently.

The complete SEM expansion for the induced surface current $\bar{J}$ as expanded in the frequency domain as described by Pearson [6] is

$$\bar{J}(\bar{r},s) = \sum_m \sum_i \beta_{mi}\eta_{mi}\bar{J}_{mi}(\bar{r})(1/(s-s_{mi}) + 1/s_{mi}) \qquad (2.22a)$$

where β_{mi} is the SEM normalization constant defined by

$$\beta_{mi} = <\bar{J}_{mi}(\bar{r}');\partial/\partial s(\bar{\bar{\Gamma}}_m(\bar{r},\bar{r}',s_{mi});\bar{J}_{mi}(\bar{r}')>^{-1} \qquad (2.22b)$$

and where η_{mi} is a SEM coupling coefficient defined by

$$\eta_{mi} = <\bar{J}_{mi}(\bar{r},s_{mi});\bar{E}^{inc}(\bar{r},s_{mi})> . \qquad (2.22c)$$

It should be pointed out at this point that solutions to eq.(2.21), which is a harmonic-by-harmonic solution to the homogeneous form of eq.(2.7), are also solutions to eq.(2.7). Therefore, poles and natural modes of eq.(2.18) are also the poles and natural modes of eq.(2.7).

The numerical method used to determine the SEM quantities described above follows that of Glisson and Wilton for a general body of revolution [8]. The location in the complex plane of the poles (natural resonances) of the surface current density function $\bar{J}(z,\phi,s)$, as represented by (2.22a) is of primary importance, if the this representation is to be used in the characterization of the induced surface current. For the purposes of computation, (2.18) may be formulated as a matrix equation by the expansion of the unknown current using a method of moments formulation as described by Harrington [10]. Eq.(2.18) can be written as the square system of equations

$$\overline{\overline{[Z_m(s)]}}\,\overline{[J_m(s)]} = \overline{[V_m(s)]} \qquad (2.23)$$

where $\overline{\overline{[Z_m(s)]}}$ is the system impedance matrix and where $\overline{[J_m(s)]}$ and $\overline{[V_m(s)]}$ are the response and source vectors respectively. In order to solve for the natural resonant frequencies, where the incident E field is zero, eq.(2.23)

becomes

$$\overline{\overline{[Z_m(s_{mi})]}}\,\overline{[J_{mi}]} = 0, \tag{2.24}$$

to yield s_{mi}, which are the numerical estimates to the natural resonant frequencies for (2.24) to have a non-trivial solution, the determinant of $\overline{\overline{[Z_m(s)]}}$ must vanish at these frequencies. Therefore, in order to determine the natural resonances of the current for the open-ended cylinder, the following equation must be solved

$$\det\overline{\overline{[Z_m(s)]}} \equiv \Delta(s) = 0. \tag{2.25}$$

A few observations about the location and nature of the natural resonances can be inferred from (2.25) and the analogy to circuit theory as Tesche [11] points out. The resonances must lie in the left-hand portion of the s-plane, since the time behavior of the current is as e^{st}, and an exponential growth for the current is not physically possible on a passive scatterer. Also, since the time domain current is real, the poles must either occur in conjugate pairs, or be purely real. It is also assumed that all of the poles are simple poles. Since the natural resonances of the current can be determined from the zeros of the determinant of the impedance matrix and since it is analytic in s, the contour integration method due to Singaraju et.al. can be applied to evaluate the

zeros of the analytic function [12]. In this approach, Cauchy's residue theorem is used to find the number of zeros in a given contour and a simple extention of this theorem allows the location of the zeros to be determined. As stated in [12], the major advantage of this method over the earlier methods of finding the zeros, which was an iterative method such as Muller and Newton-Raphson [11], is that, with this method, no previous knowledge of the approximate location of the zero of the complex function is needed. The contour method of searching for pole locations is exhaustive if applied carefully, whereas, with the iterative method, one could easily overlook a pole. Also if the complex function has an exponential behavior, which this one does, the iterative method is more unreliable. All of the poles or natural resonances presented in this report were found using the CONTOUR and SEEK subroutines contained in [12].

The current which exists for a zero forcing function at singular points s_{mi} has been referred to as a current natural mode $[J_{mi}(z)]$ which is the solution to eq.(2.24). Therefore, to obtain the natural current mode, the homogeneous solution to (2.23) must be obtained. $[J_{mi}(z)]$ is in general a complex quantity which has an arbitrary magnitude. For convenience, the current natural modes have been normalized in terms of the magnitude of the symmetric product of the modes. The symmetric product has previously been defined in (2.13) as

$$\langle \bar{F} \cdot \bar{G} \rangle = \iint_S \bar{F} \cdot \bar{G} \, dS \qquad (2.26)$$

where S is the surface of the open-ended cylinder. The two components of current can be defined as

$$J_{zmi}(\phi,z) = (1/\pi) J_{zmi}(z) \cos(m\phi) \qquad (2.27a)$$

$$J_{\phi mi}(\phi,z) = (j/\pi) J_{\phi mi}(z) \sin(m\phi) \, , \qquad (2.27b)$$

substituting (2.27a) and (2.27b) into (2.26) and specializing the surface integration to the cylinder (2.26) becomes

$$\langle \bar{J}_{mi}; \bar{J}_{mi} \rangle = (a/\pi) \int_{-h}^{h} [J^2_{zmi}(z') - J^2_{\phi mi}(z')] \, dz \qquad (2.28)$$

using a substitution of variable $z=2h\zeta$ and the definition of aspect ratio

$$\alpha = h/a = L/2a \qquad (2.29)$$

where h is the half-length and a is the radius, then (2.28) becomes

$$\langle \bar{J}_{mi};\bar{J}_{mi} \rangle = (2ha/\pi) \int_{-.5}^{.5} [J^2_{zmi}(\zeta L) - J^2_{\phi mi}(\zeta L)]\, d\zeta$$

$$= (L^2/2\pi a) \int_{-.5}^{.5} [J^2_{zmi}(\zeta L) - J^2_{\phi mi}(\zeta L)]\, d\zeta \,. \qquad (2.30)$$

Defining the surface area as

$$S = L(2\pi a) = \pi L^2/\alpha \qquad (2.31)$$

then substituting into (2.30), it becomes

$$\langle \bar{J}_m;\bar{J}_m \rangle = (S/2\pi^2) \int_{-.5}^{.5} [J^2_{zmi}(\zeta L) - J^2_{\phi mi}(\zeta L)]\, d\zeta. \qquad (2.32)$$

Choosing

$$(I/2\pi^2) \int_{-.5}^{.5} [J^2_{zmi}(\zeta L) - J^2_{\phi mi}(\zeta L)]\, d\zeta = I$$

the normalized currents can then be calculated by

$$\tilde{J}_{zm}(\zeta L) = \pi J_{zmi}(\zeta L)/|H| \qquad (2.33a)$$

$$\tilde{J}_{\phi m}(\zeta L) = \pi J_{\phi mi}(\zeta L)/|H| \qquad (2.33b)$$

where

$$H_{mi}^{Z} = \int_{0}^{-S} [J_{zmi}^{Z}(\zeta L) - J_{\phi mi}^{Z}(\zeta L)]\, d\zeta \,.$$

To complete the SEM description, the normalization constant must be calculated. Recalling from eq.(2.22b) the definition of the normalization constant

$$\beta_{mi} = \langle \bar{J}_{mi}(\bar{r}'); \partial/\partial s(\bar{\bar{\Gamma}}_{m}(\bar{r},\bar{r}',s_{mi}); \bar{J}_{mi}(\bar{r}') \rangle^{-1} \,. \qquad (2.34)$$

The only term in (2.34) which is still unspecified is the term involving the derivative of the impedance matrix with respect to s. This may be done analytically and the details of the analysis for the derivative terms in (2.34) are given in Appendix A. Substituting the results of Appendix A, along with the natural modes, into eq.(2.34) the normalization constant can be determined.

In order to solve eq.(2.18), a method of moments approach which follows Glisson and Wilton's approach in [8] was used. The generating arc is segmented into a sequence of linear segments as shown in Figure 2, where the generating arc is considered to be contained in the $\phi=0$ plane. The segmented generating arc can be rotated about the axis of rotation to produce the surface of the cylinder. The unknown electric currents which are induced

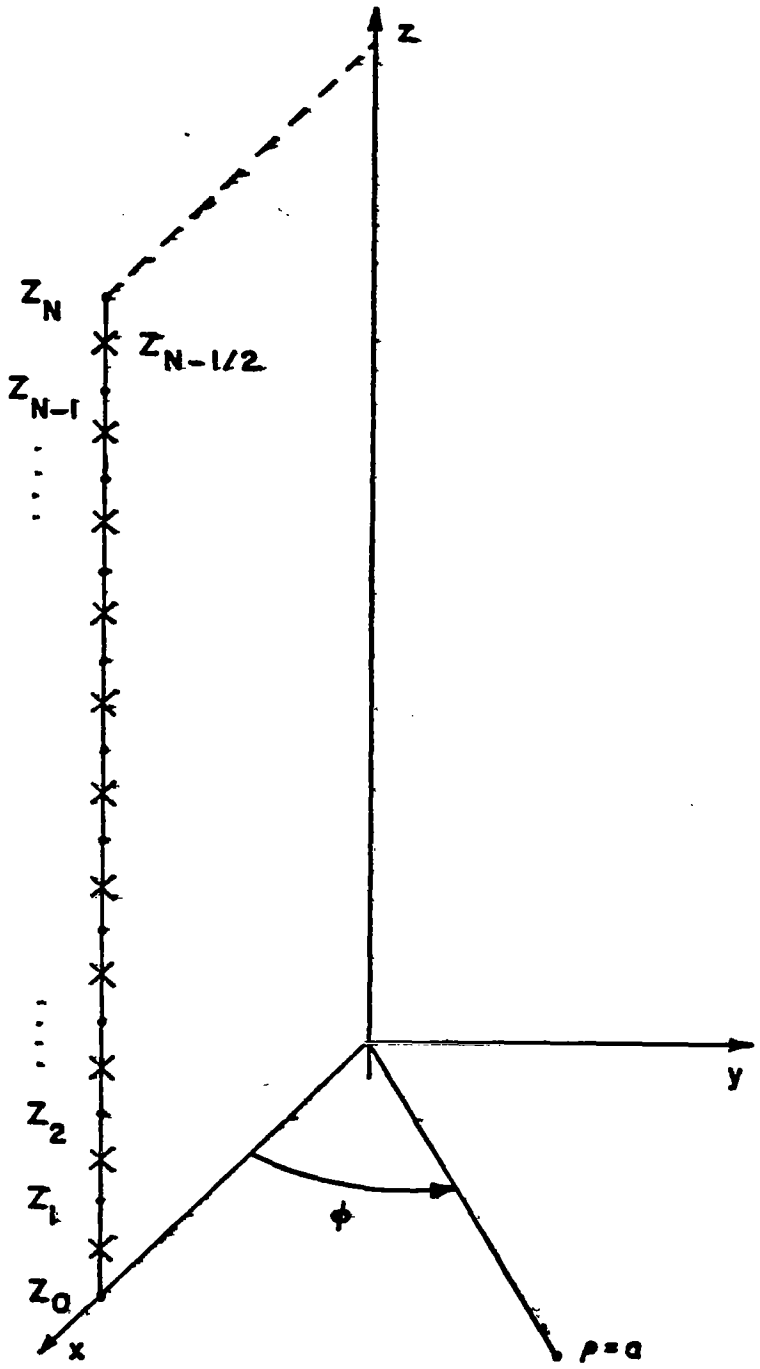

Figure 2. Segmentation of the generating arc for purposes of numerical computation.

on the surface can now be approximated by pulse functions in the axial ($\hat{a}_z$) direction.

The expansion of the electric current may be written as

$$\bar{J}_m(\rho,\phi,z) = \sum_{n=1}^{N-1} J_{zm}^n P_1^n(z')\hat{a}_z + \sum_{n=1}^{N} J_{\phi m}^n P_2^n(z')\hat{a}_\phi \qquad (2.35)$$

where

$$P_1^n(z') = \begin{cases} 1 \ , z_{n-\frac{1}{2}} \le z' \le z_{n+\frac{1}{2}} \\ 0 \ , \text{otherwise} \end{cases} \qquad (2.36a)$$

and

$$P_2^n(z') = \begin{cases} 1 \ , z_{n-1} \le z \le z_n \\ 0 \ , \text{otherwise} . \end{cases} \qquad (2.36b)$$

The charge contribution which comes from the derivative of J_z with respect to z can be approximated as

$$\partial/\partial z'(J_{zm}(z')) = \sum_{n=1}^{N} \left\{ \frac{J_{zm}^n - J_{zm}^{n-1}}{|z_n - z_{n-1}|} \right\} P_2^n(z') \qquad (2.37)$$

where it is assumed in (2.37) that

$$J^0_{zm} \equiv J^N_{zm} = 0.$$

This is the so-called "staggered zoning scheme" expansion of the current and charge of Wilton et.al. [13]. This scheme has proven well-suited for numerical solutions of problems involving edges and two non-zero components of current. The features of staggered zoning which provide its utility in this context are discussed in [13].

The testing functions can be defined as

$$T^q_{1m}(z) = \delta^q_{1m}(z) \tag{2.38a}$$

$$T^q_{2m}(z) = \delta^q_{zm}(z) \tag{2.38b}$$

where

$$\delta^q_{1m}(z) = \begin{cases} 1 \ , z=z_q \\ 0 \ , \text{otherwise} \end{cases} \tag{2.39a}$$

$$\delta^q_{2m}(z) = \begin{cases} 1 \ , z=z_{q-\frac{1}{2}} \\ 0 \ , \text{otherwise.} \end{cases} \tag{2.39b}$$

Testing eq.(2.18a) with (2.38a) and eq.(2.18b) with (2.38b) yields

$$E^{inc}_{zm}(z_q) = \beta^{qn}_{11m}(J_{zm}) + \beta^{qn}_{12m}(J_{\phi m}) \tag{2.40a}$$

$$E^{inc}_{\phi m}(z_q) = \beta^{qn}_{21m}(I_{zm}) + \beta^{qn}_{22m}(I_{\phi m}). \qquad (2.40b)$$

The generalized impedance matrix, consisting of β^{qn}_{ijm} can now be expressed, where the subscript m refers to the Fourier coefficient and the q and n superscripts refer to field and source points, respectively. As a matter of convenience in presenting the expressions the following integral will be defined as

$$K(z_1, z_2, z_q, m) = \int_{z_1}^{z_2} G_m(z_q, z')\, dz' \qquad (2.41)$$

where G_m is defined by (2.17). The natural modes on the structure can be partitioned into two symmetry classes -- one associated with a magnetic image plane and one associated with an electric image plane.

Using these symmetry properties and the previous definitions, the operators in (2.19) can be expressed as follows:

$$\beta^{qn}_{11m} = -\frac{a}{4\pi s\varepsilon \Delta z^2}\,[K(z_{n-\frac{1}{2}}, z_{n+\frac{1}{2}}, z_{q+1}, m) - (2 + (s\Delta z/c)^2)K(z_{n-\frac{1}{2}}, z_{n+\frac{1}{2}}, z_q, m) + K(z_{n-\frac{1}{2}}, z_{n+\frac{1}{2}}, z_{q-1}, m) \pm K(-z_{n+\frac{1}{2}}, -z_{n-\frac{1}{2}}, z_{q+1}, m) \mp (2 + (s\Delta z/c)^2)K(-z_{n+\frac{1}{2}}, -z_{n-\frac{1}{2}}, z_q, m) \pm K(-z_{n+\frac{1}{2}}, -z_{n-\frac{1}{2}}, z_{q-1}, m)\,]; \qquad (2.42a)$$

$$\beta_{12m}^{qn} = -\frac{jm}{\Delta z 4\pi s\varepsilon}\left[K(z_{n-\frac{1}{2}}, z_{n+\frac{1}{2}}, z_{q+1}, m) - K(z_{n-\frac{1}{2}}, z_{n+\frac{1}{2}}, z_q, m)\right.$$

$$\left. \mp K(-z_{n+\frac{1}{2}}, -z_{n-\frac{1}{2}}, z_{q+1}, m) \pm K(-z_{n+\frac{1}{2}}, -z_{n-\frac{1}{2}}, z_q, m)\right] ; \qquad (2.42b)$$

$$\beta_{21m}^{qn} = -\frac{jm}{\Delta z 4\pi s\varepsilon}\left[K(z_{n-\frac{1}{2}}, z_{n+\frac{1}{2}}, z_q, m) - K(z_{n-\frac{1}{2}}, z_{n+\frac{1}{2}}, z_{q-1}, m)\right.$$

$$\left. \mp K(-z_{n+\frac{1}{2}}, -z_{n-\frac{1}{2}}, z_q, m) \pm K(-z_{n+\frac{1}{2}}, -z_{n-\frac{1}{2}}, z_{q-1}, m)\right] ; \text{ and} \qquad (2.42c)$$

$$\beta_{22m}^{qn} = \frac{1}{4\pi s\varepsilon}\left[\frac{s^2 a}{2c^2}\left[K(z_{n-\frac{1}{2}}, z_{n+\frac{1}{2}}, z_q, m+1) + K(z_{n-\frac{1}{2}}, z_{n+\frac{1}{2}}, z_q, m-1)\right.\right.$$

$$\left. \mp K(-z_{n+\frac{1}{2}}, -z_{n-\frac{1}{2}}, z_q, m+1) \mp K(-z_{n+\frac{1}{2}}, -z_{n-\frac{1}{2}}, z_q, m-1)\right]$$

$$\left. + \frac{m^2}{a}\left[K(z_{n-\frac{1}{2}}, z_{n+\frac{1}{2}}, z_q, m) \mp K(-z_{n+\frac{1}{2}}, -z_{n-\frac{1}{2}}, z_q, m)\right]\right] . \qquad (2.42d)$$

The upper signs refer to the electric image plane case, while the lower signs refer to the magnetic case. A detailed analysis of the handling of the singularity which occurs in the evaluation of the self terms, when the source and observation point coincide, is included in Appendix B.

2.4 Validation of Computer Code

Throughout its development, the computer code which is used to calculate the data presented here was validated against well accepted benchmark computer codes and data. The code used in the determination of the natural reso-

nances for the current was benchmarked for the zeroth and higher order mode cases. The code developed for determining the normalization constants was benchmarked only for the zeroth mode case, since there is presently no data available for the higher mode cases.

In order to validate the zeroth order mode case, which corresponds to thin wire theory, the code was run under the driven case of an incident plane wave excitation for an aspect ratio of 100. The induced current was checked against accepted results. The two were in good agreement. The code was then modified to calculate the natural resonances. Using an aspect ratio of 100, the first layer poles found by Tesche in [4] were determined. The magnitude of the poles presented in this report demonstrated agreement with the poles presented by Tesche to within 1% of their magnitude. The natural modes were determined for the cases presented by Tesche, and again, good agreement was observed. Finally, for the zeroth order case, the normalization constants were calculated and compared to the normalization constants presented by Tesche. The code presented in this report calculates the normalization constant for the current density rather than for the total current. Therefore, for comparison with Tesche, the normalization constants were renormalized to the total current rather than to the current density. The renormalized data compared to Tesche to within 2% in magnitude. The code was benchmarked for the higher azi-

muthal orders using an aspect ratio of 3.1415, for the inhomogeneous excitation due to an end-on incidence of the cylinder by a plane wave. The results were compared to the results presented by Glisson and Wilton in their Body of Revolution program. The generating arc in their formulation was specialized to represent an open-ended cylinder. The results of the two codes agreed to within three significant digits on a DEC-10 computer. The total cpu time on the DEC-10 for the Glisson and Wilton general body of revolution code was 55.06 sec, compared to the cylinder code presented here, took a total of 3.78 cpu secs. Therefore, the specialized cylinder code is almost 15 times faster than the totally general body of revolution code written by Glisson and Wilton. This is not surprising since their code allows dielectric or perfectly conducting bodies, as well as arbitrarily shaped bodies. However, to be cost-effective for the determination of the SEM parameters for a thick cylinder, the present, a more efficient code is required.

Further validation of the cylinder code was performed by specializing the cylinder to a ribbon loop. The poles of the ribbon loop were compared to the poles or the circular wire loop presented by Umashankar and Wilton in [14]. The two loops were chosen so that they had equal surface area as seen in Figure 3. The pole value calculated from the ribbon loop was -0.0148 + j0.0893. The pole value of the wire loop is reported to be -0.0131 + j0.0889

after renormalizing the pole value to $sL/c\pi$. The poles for the different geometries cannot be compared directly, but the degree of proximity here is quite gratifying.

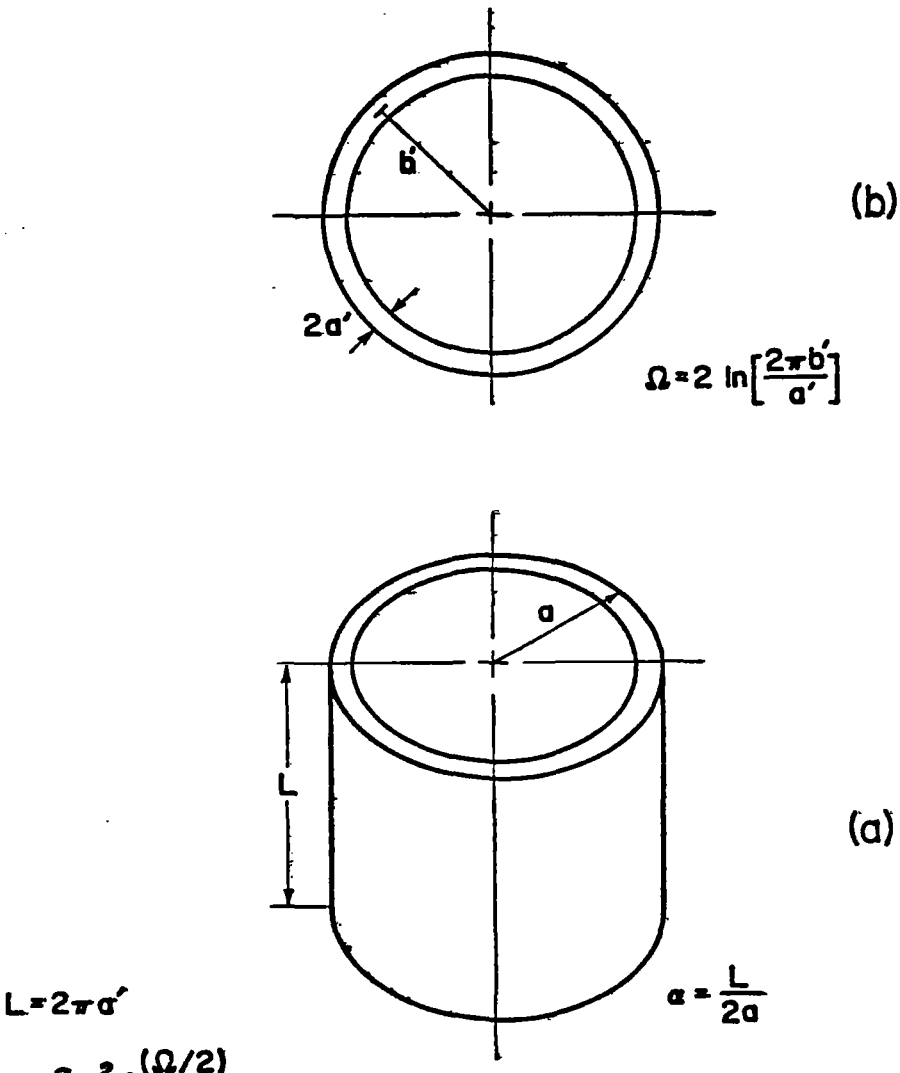

Figure 3. Comparison of ribbon loop geometry (a) to wire loop geometry (b), where they were chosen to have equal surface area.

CHAPTER 3

INTERPRETATION OF RESULTS

This chapter presents the SEM parameters for various thicknesses of open-ended cylinders. The poles are presented for azimuthal harmonic varations of m=0, 1, and 2. Selected natural modes are presented to represent the compiled data. These data were obtained by implementing the formulations presented in the previous chapter.

The trajectories of the natural resonances for the structure as its aspect ratio is varied from 100 to 3.33 is seen in Figure 4. Aspect ratio is defined as the length-to-diameter ratio for the cylinder as indicated in the inset in the Figure. Figure 4.a shows the pole locations for the m=0 case (constant azimuthal current variation) over the range of aspect ratios. It is observed from Figure 4.a that the poles tend to move downward and outward, which correspond to a decrease in resonant frequency and an increase in the damping factor, as the cylinder gets thicker. Of course, these results are essentially those of Tesche [4] extended to lower aspect ratios and this tendency in the trajectory agrees with his observation. Said differently, the quality factor

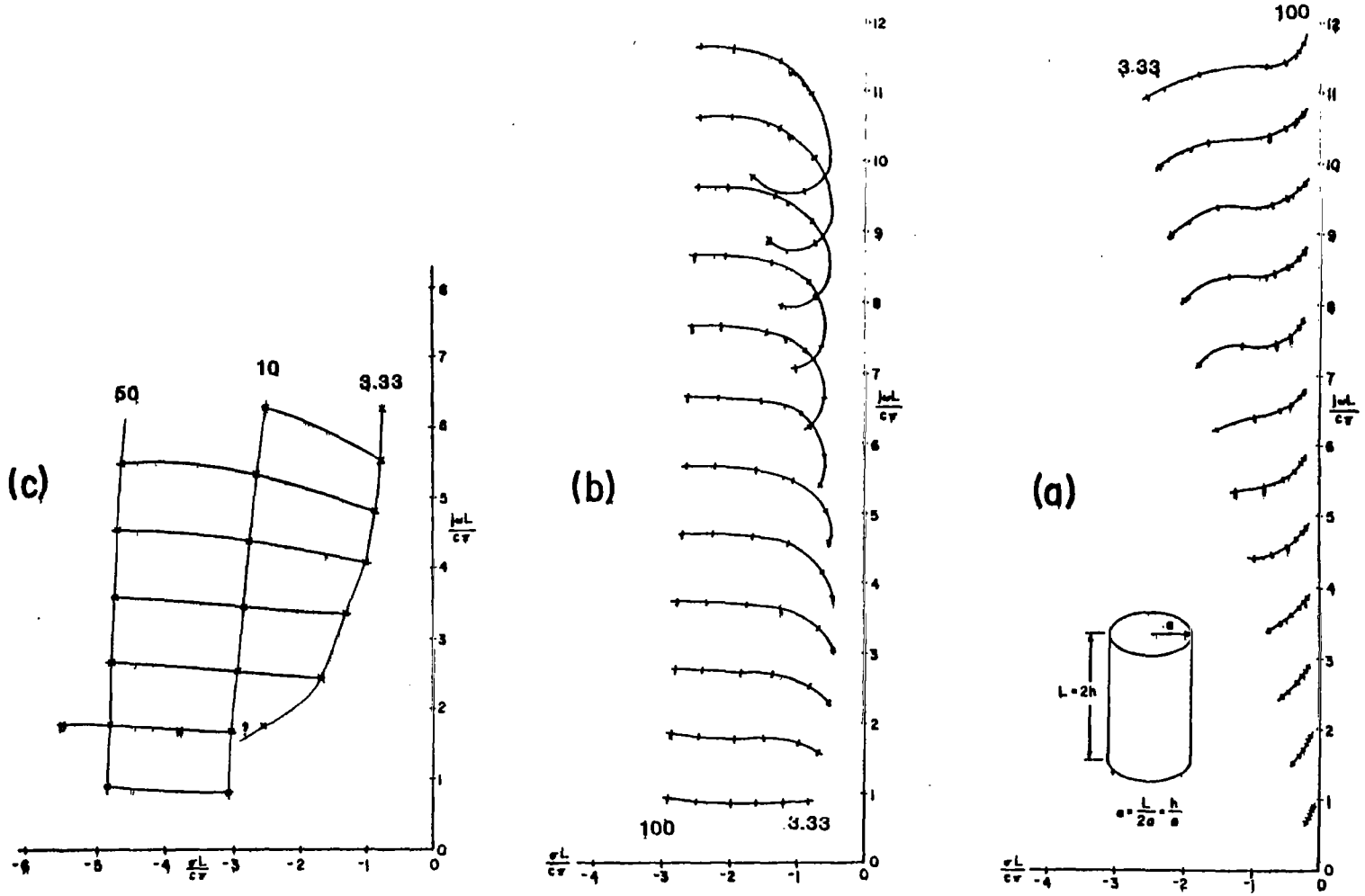

Figure 4. Pole trajectories for cylinder aspect ratios ranging from 100 to 3.33: (a) zeroth azimuthal harmonic set; (b) first harmonic set; (c) second harmonic set. Ticks on trajectories represent evaluations at aspect ratios 100, 50, 20, 10, 5, and 3.33.

(Q) for the m=0 modes decreases with decreasing aspect ratio. This decreasing-Q phenomenon is quite pronounced for the higher resonances of the extremely fat cases.

The open cylinder possesses a second independent set of m=0 modes. It is clear from (2.19) that $\beta_{120} = \beta_{210} = 0$ so that the J_z and J_ϕ components of current are decoupled in the m=0 case. Futhermore, the operators β_{110} and β_{220} exhibit singularities with respect to s independently of one another. The m=0 poles discussed in the preceding paragraph are, in fact those of β_{110} -- i.e. those associated with resonances in longitudinal current flow. The resonances attributable to β_{220} are counterpart to the m=0 resonances of a loop structure as, for example, [14] reports. These loop resonances cannot be excited by a time harmonic excitation as a consequence of their azimuthal invariance. We, therefore, do not address them further here.

The pole trajectories for the case of first harmonic azimuthal variation are displayed in Figure 4b. The direction of migration here is seen to be that of increasing Q with decreasing aspect ratio-- the reverse of that for the zeroth-harmonic case. This phenomenon is the result of the torsional paths which the currents follow for the m=1 amd higher azimuthal order cases. Figure 5 displays qualitatively the paths of current over the unrolled cylinder surface for different rates of azimuthal and longitudinal variation. (We point out that the por-

trayals in the Figure are not computed from the modes and are, indeed, quite simplistic representations introduced here for interpretive purposes.) For the m=0 modes there is no circumferential current component and the flow lines are along straight line paths. The involvement of the circumferential component for modes higher than zeroth-order introduces a torsional component to the streamlines. The charge movements constituting the m=0 modal currents undergo acceleration only at the ends of the structure.

The modes with higher-order azimuthal variation impose a continual centripetal acceleration on the charge. This acceleration imposes a continual shedding of energy to radiation at appreciable levels. Comparison of Figures 6a and 6b substantiates this observation. The data in Figure 6 are simply the α=3.33 aspect ratio results extracted from the trajectories given in Figure 5. (A few additional poles appear in Figure 6 and are subsequently discussed.) The damping of the resonances is observed to increase with increasing azimuthal order for the lower-frequency resonances. That is, the increasing of torsion with damped resonances. A more careful observation indicates, however, that this trend does not persist further up in the complex plane. The current paths become quite complex and somewhat localized due to the higher order longitudinal variation associated with these poles and have not admitted to a consistent interpretation, to date.

The migration of the poles in a direction of increas-

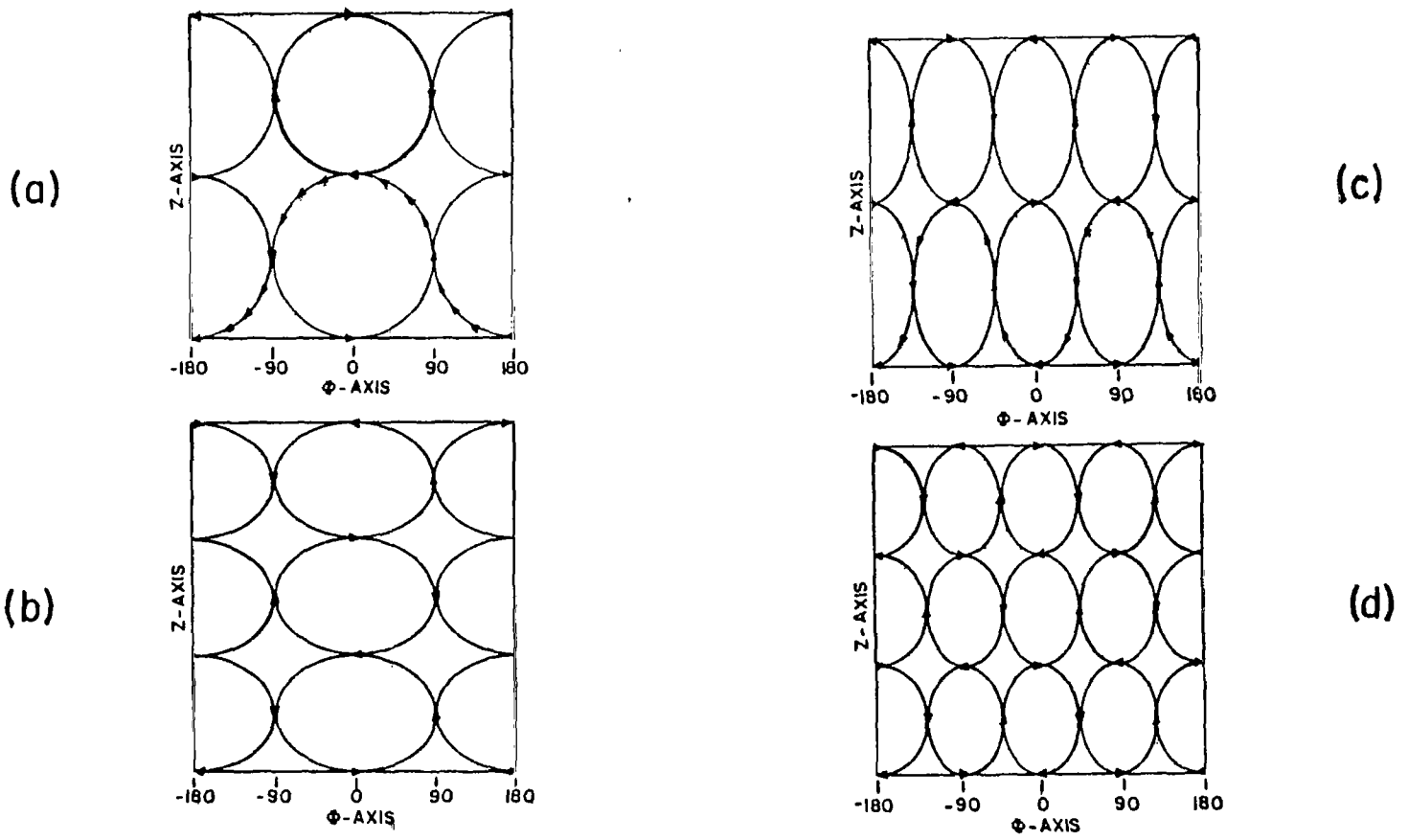

Figure 5. Qualitative current flow lines for specimen natural modes plotted on the unrolled cylinder surface: (a) m = 1 harmonic, first mode; (b) m = 1 harmonic, second mode; (c) m = 2 harmonic, first mode; and (d) m = 2 harmonic, second mode. Observe that rate of variation increases, respectively, with mode number and with harmonic number.

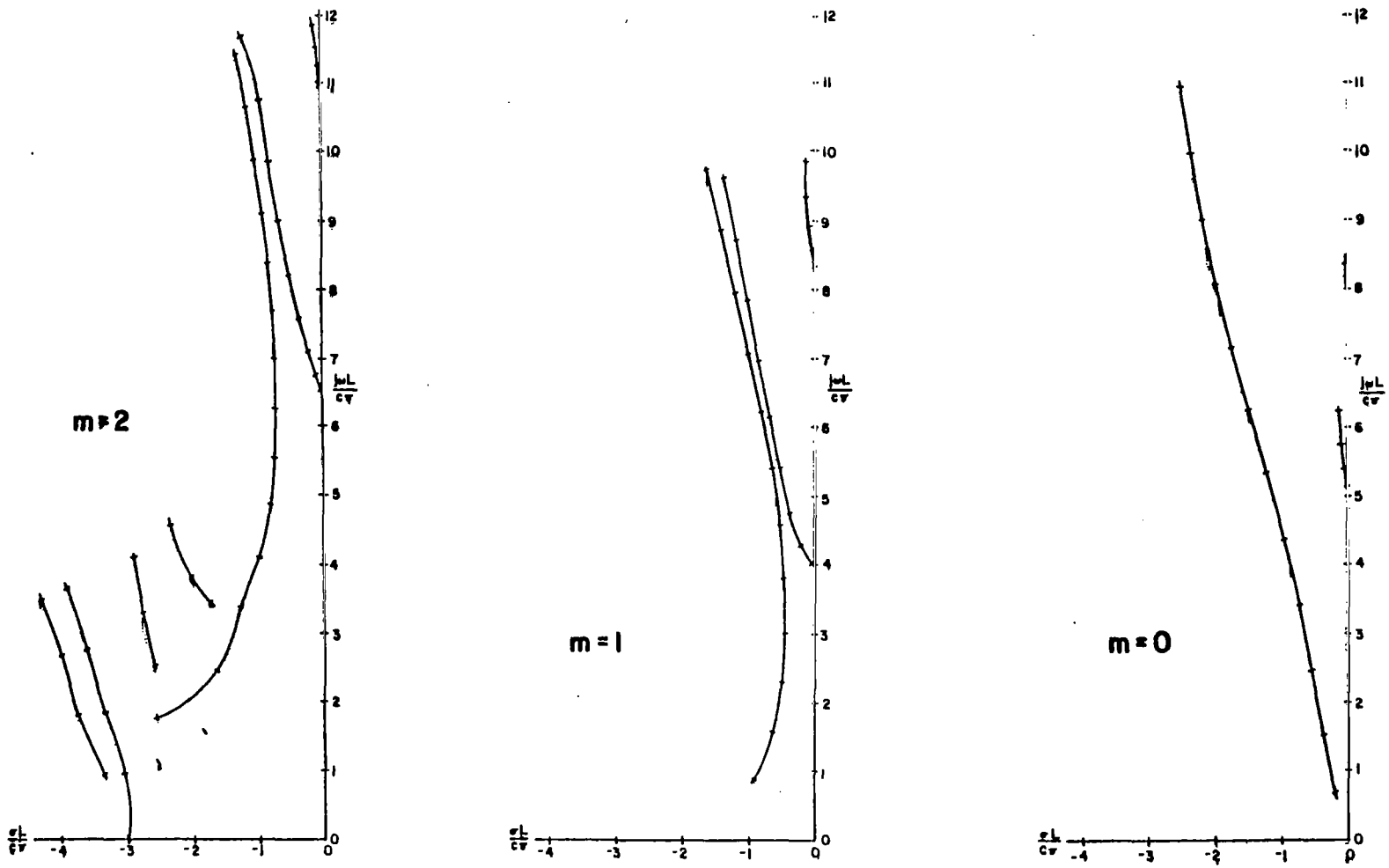

Figure 6. The family of poles for $\alpha = 3.33$ for the $m = 0$, $m = 1$, $m = 2$ harmonic modes.

ing Q with decreasing aspect ratio evidenced by the m=1 and m=2 poles in Figure 5 is due to the decreasing of torsion with increasing circumference, thereby reducing the rate of radiation as charge flows along the cylinder. This trend is contrary to the direction of migration in the m=0 case.

Figure 6 includes additional sets of poles, which are deleted from Figure 5 for the sake of clarity. These poles are arranged in "layers" which emerge near the jω axis and are those which Wilton conjectures to be interior waveguide mode cavity resonances, radiation through the apertures at the open ends of the cylinder [17]. They correspond with the so-called type III poles of the thin-wire loop.

This conjecture is substantiated by the comparison of the pole locations with the jω axis resonances of a cylindrical cavity formed by an electric-walled cylinder and terminated with magnetic walls closing the ends of the cylinder.

TABLE I

CYLINDRICAL WAVEGUIDE RESONANCES

	TM_{01p}	TM_{11p}	TM_{20p}	TM_{21p}
p = 1	5.20	1 8.19	1 11.76	1 10.94
2	5.48	2 8.38	2 11.88	2 11.08
3	5.92	3 8.67	3 12.09	3 11.61
4	6.48	4 9.06	4 12.38	4 11.99

	TE_{01p}	TE_{11p}	TE_{21p}
p = 1	8.19	1 4.03	1 6.56
2	8.37	2 4.39	2 6.78
3	8.67	3 4.93	3 7.14
4	9.06	4 5.59	4 7.61

Table I gives the resonant frequency values for the first several modes of this cavity normalized to $L/c\pi$ as the frequency variables are in Figure 6 and for the $\alpha=3.33$ aspect ratio of the Figure. Comparing the values in the Table with the pole value in Figure 6a we see a layer emerging near the normalized first resonant frequency 5.18 of the TM_{011} mode of the cavity. The second pole in this layer lies slightly to the left of the value 5.40, while the TM_{012} resonance falls at 5.48. Because of the interaction of the frequency dependence of the admittance of the radiating circular apertures at the ends of the cylinder we would not expect a close agreement for these "radiating waveguide poles" and the cavity poles. Nevertheless, the association of this layer with the TM cavity modes is clear. In like fashion, we may identify the following associations:

a layer emerging near $j\omega = 4$ in Figure 6a with the TE_{01p} modes;

a layer emerging near $j\omega = 4$ in Figure 6b with the TE_{11p} modes;

a layer emerging near $j\omega = 8.35$ in Figure 6b with the TM_{11p} modes;

a layer emerging near $j\omega = 6.5$ in Figure 6c with the TE_{21p} modes; and

a layer emerging near $j\omega = 11$ in Figure 6c with the TM_{21p} modes.

The consistancy of these associations strongly supports the Wilton conjecture in [17]. One further observation is appropriate here. As the aspect ratio decreases to zero,

the structure collapses to a ribbon loop. The natural resonances of a specimen ribbon loop were computed and compared to those of a counterpart thin-wire loop. All three types described by Umashankar and Wilton [14] were present.

The current natural modes for the first two exterior poles for a relatively thick cylinder (α=10) are displayed in Figures 7 through 11 and for a relatively thin cylinder (α=50) are presented in Figures 12 through 16. *Harmonic modes m=0, 1, and 2 are presented. Figure 7 and Figure 12 present a graphical representation of the real and imaginary parts of the z dependent factor of the natural modes for the (α=10), and (α=50) case, respectively. This representation of the natural modes for the (m=0) case agree well with Tesche's modes [4]. It can be observed from these Figures that the real part of the mode for the first pole exhibits one-half period of something akin to a sinusoidal function, the real part of the mode for the second pole exhibits two-half periods of something akin to a sinusoidal function. This well-known trend continues for higher pole numbers in the m=0 case.

For the case where m=1, Figures 8 and 9 and Figures

---

* The numerical value for the normalized pole $sL/c\pi$ and normalized normalization constant $\beta L/c$ are tabulated above each graph. The zeroth modes are normalized on a peak magnitude basis, while the higher order modes are normalized according to (2.33). The normalizations are discussed explicitly and in more detail in Appendix C.

13 and 14 present the real and imaginary part of the natural modes along with the three dimension plot of the mode above the unrolled cylinder, for (α=10) and (α=50), respectively. The (a) parts of Figures 8 and 9 and Figures 13 and 14 represent the z variation in the z directed current, where the (b) parts represent the z-variation in the azimuthally directed current. No specific pattern among the features of the various natural modes is evident for the m=1 case. However, as the cylinder gets thinner, increasing the damping factor, an apparent spreading of the energy in the mode toward the edges is seen. This is evident in the first pole for the m=1 case.

Figures 11, 15, and 16 convey the same information as Figures 8,9,13, and 14 except for the case of m=2. Again no specific trend is observed for the m=2 case except, perhaps the concentrating of the longitudinal component of current near the ends of the structure as the damping factor associated with the mode increases. This is evident, for example between Figures 10 and 15.

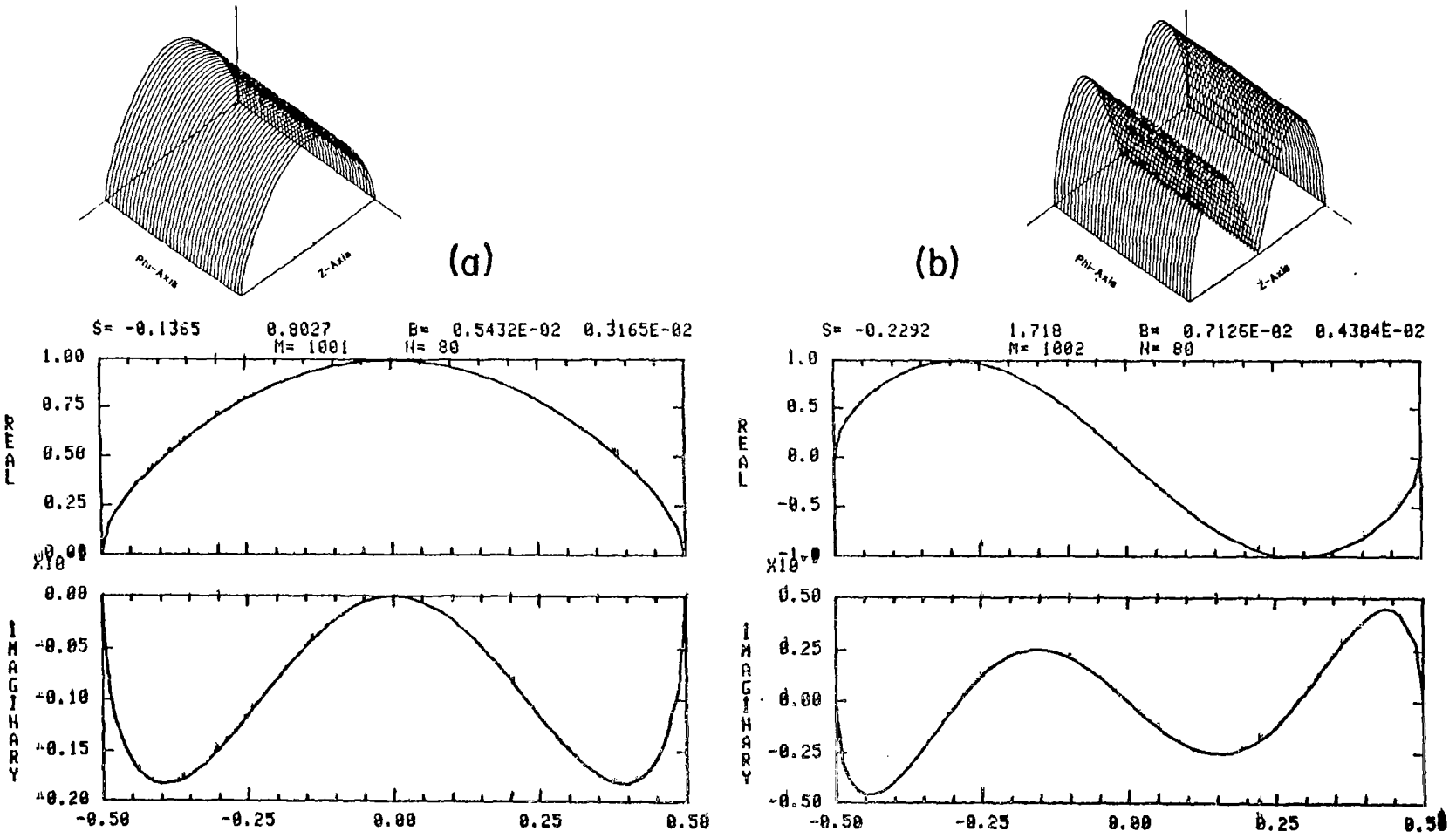

Figure 7. Characterization of the modes associated with the m = 0 harmonic, (a) first pole, (b) second pole, and aspect ratio $\alpha = 10$. The z-dependent factor of the modal current is displayed along with a three-dimensional magnitude representation of the dependence on z and ϕ over the unrolled cylinder.

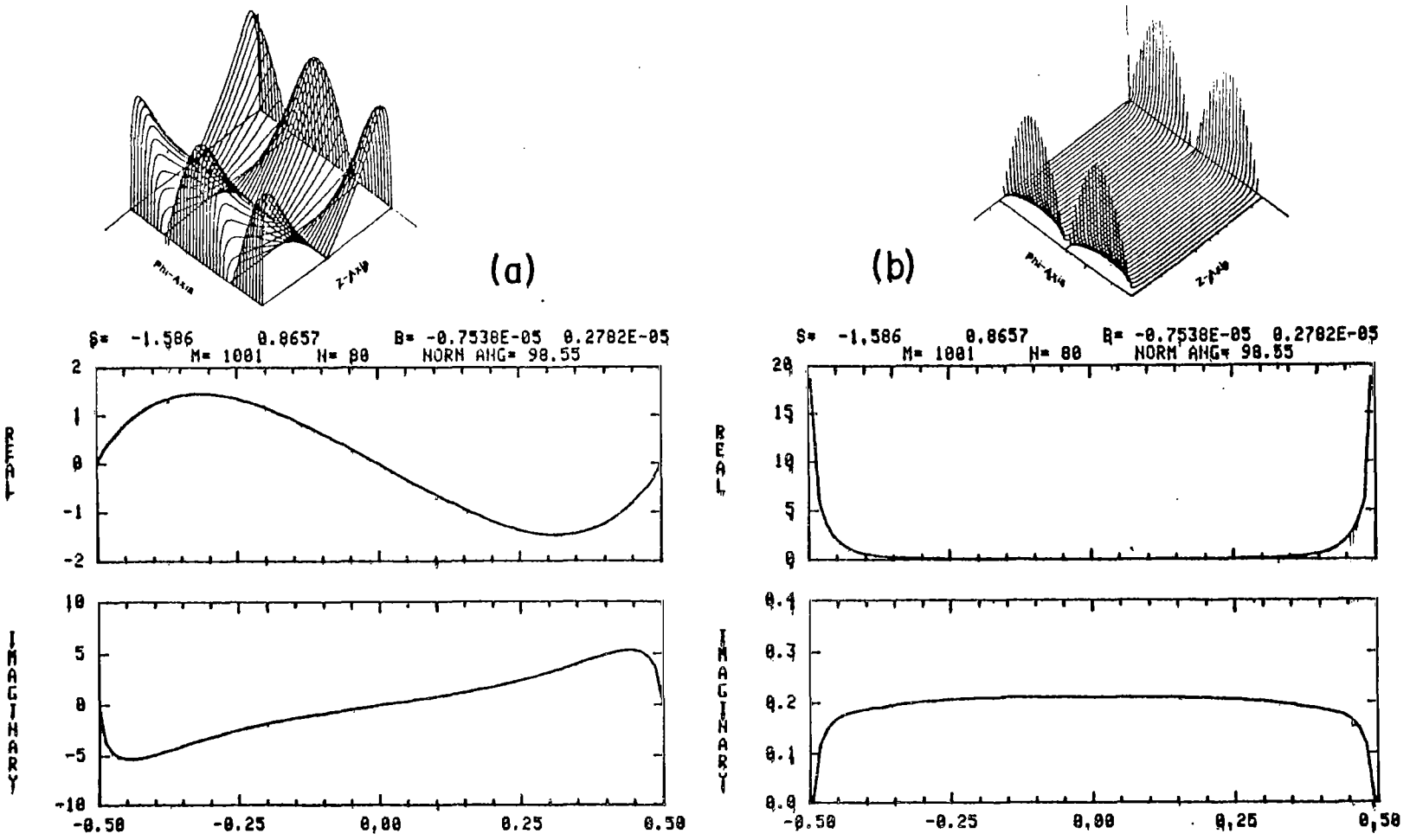

Figure 8. Characterization of the mode associated with the m = 1 harmonic, first pole, and aspect ratio $\alpha = 10$. (a) z-component of current, (b) ϕ-component of current. The z-dependent factor of the modal current is displayed along with a three-dimensional magnitude representation of the dependence on z and ϕ over the unrolled cylinder.

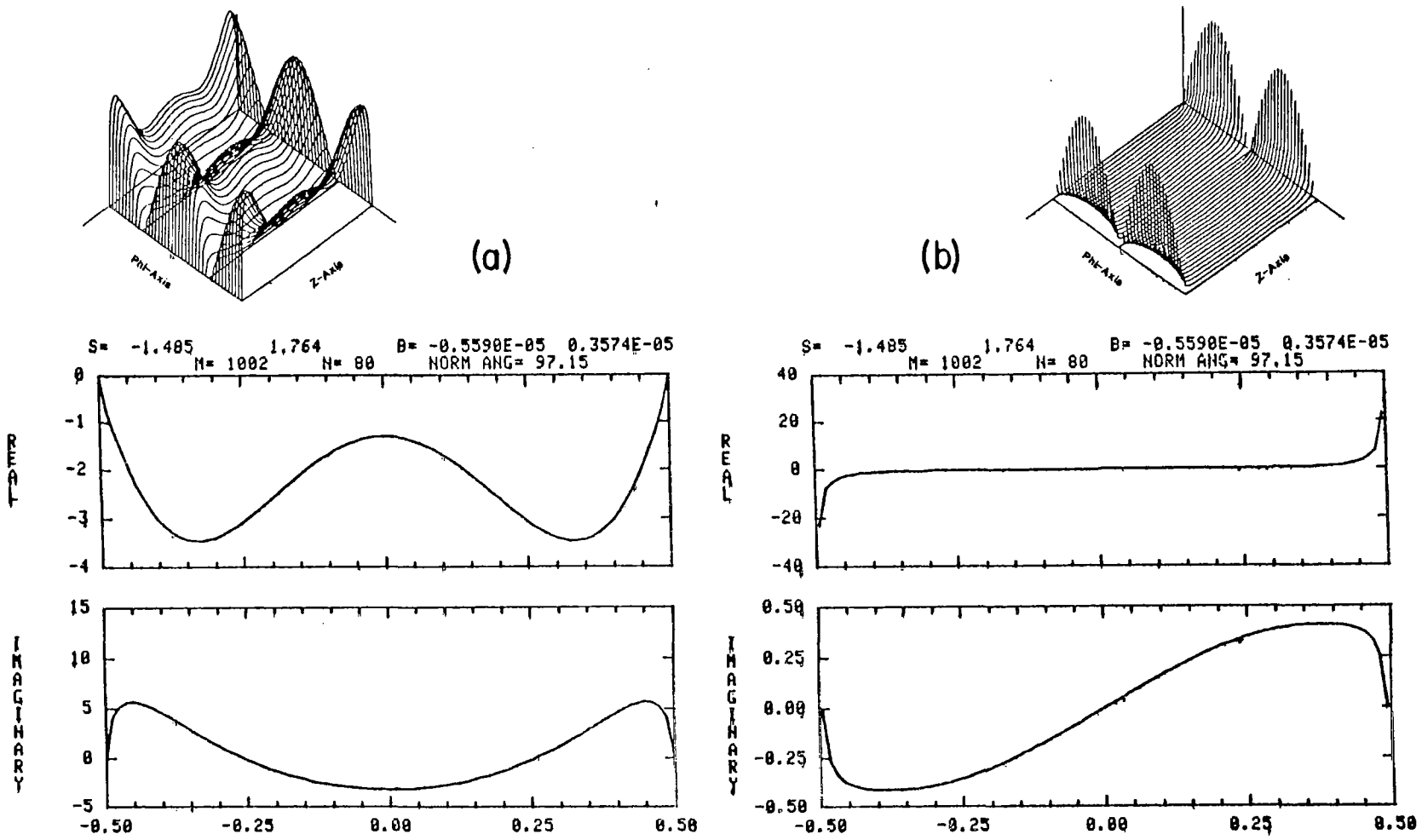

Figure 9. Characterization of the mode associated with the m = 1 harmonic, second pole, and aspect ratio $\alpha = 10$. (a) z-component of current, (b) ϕ-component of current. The z-dependent factor of the modal current is displayed along with a three-dimensional magnitude representation of the dependence on z and ϕ over the unrolled cylinder.

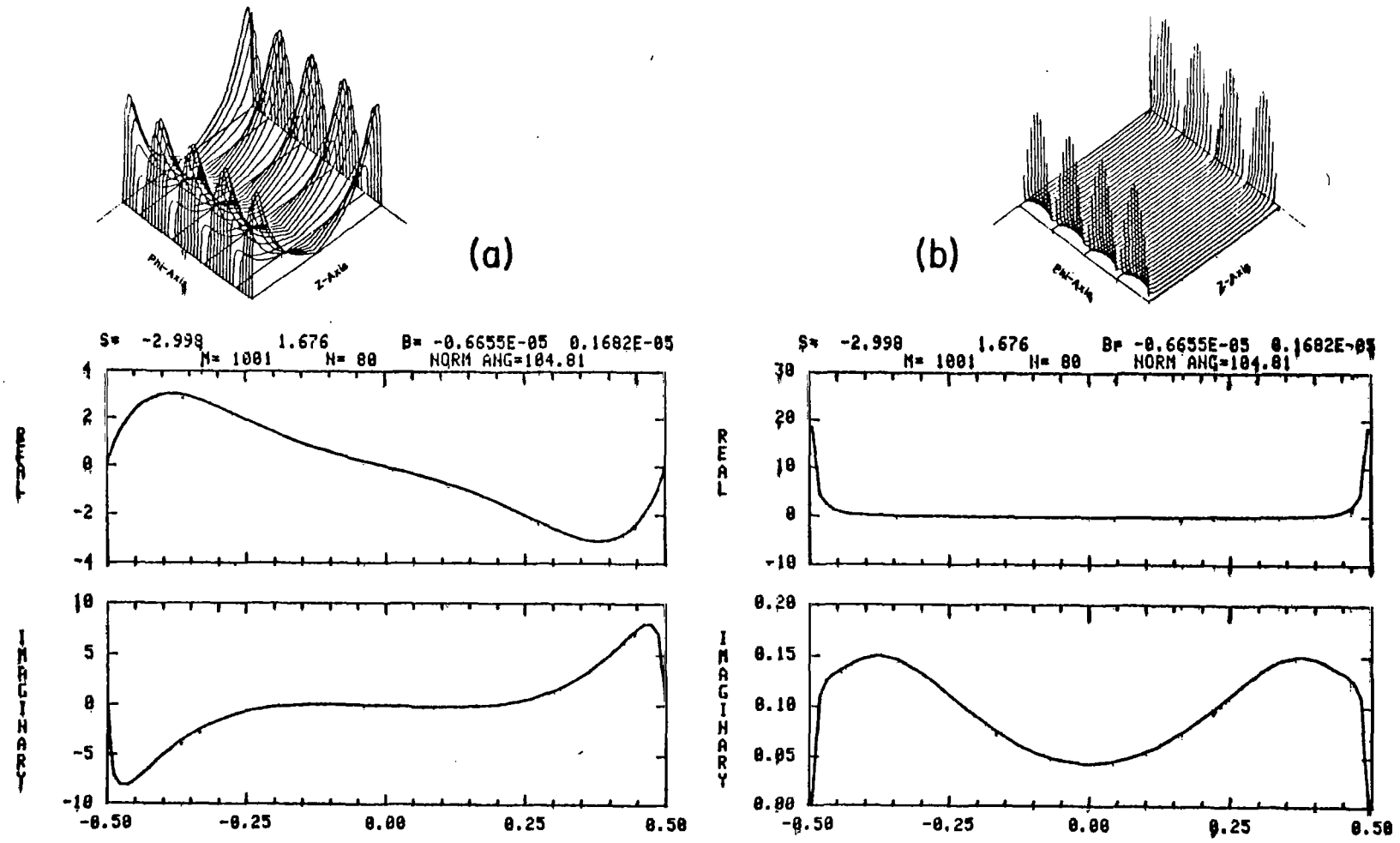

Figure 10. Characterization of the mode associated with the m = 2 harmonic, first pole, and aspect ratio $\alpha = 10$. (a) z-component of current, (b) ϕ-component of current. The z-dependent factor of the modal current is displayed along with a three-dimensional magnitude representation of the dependence on z and ϕ over the unrolled cylinder.

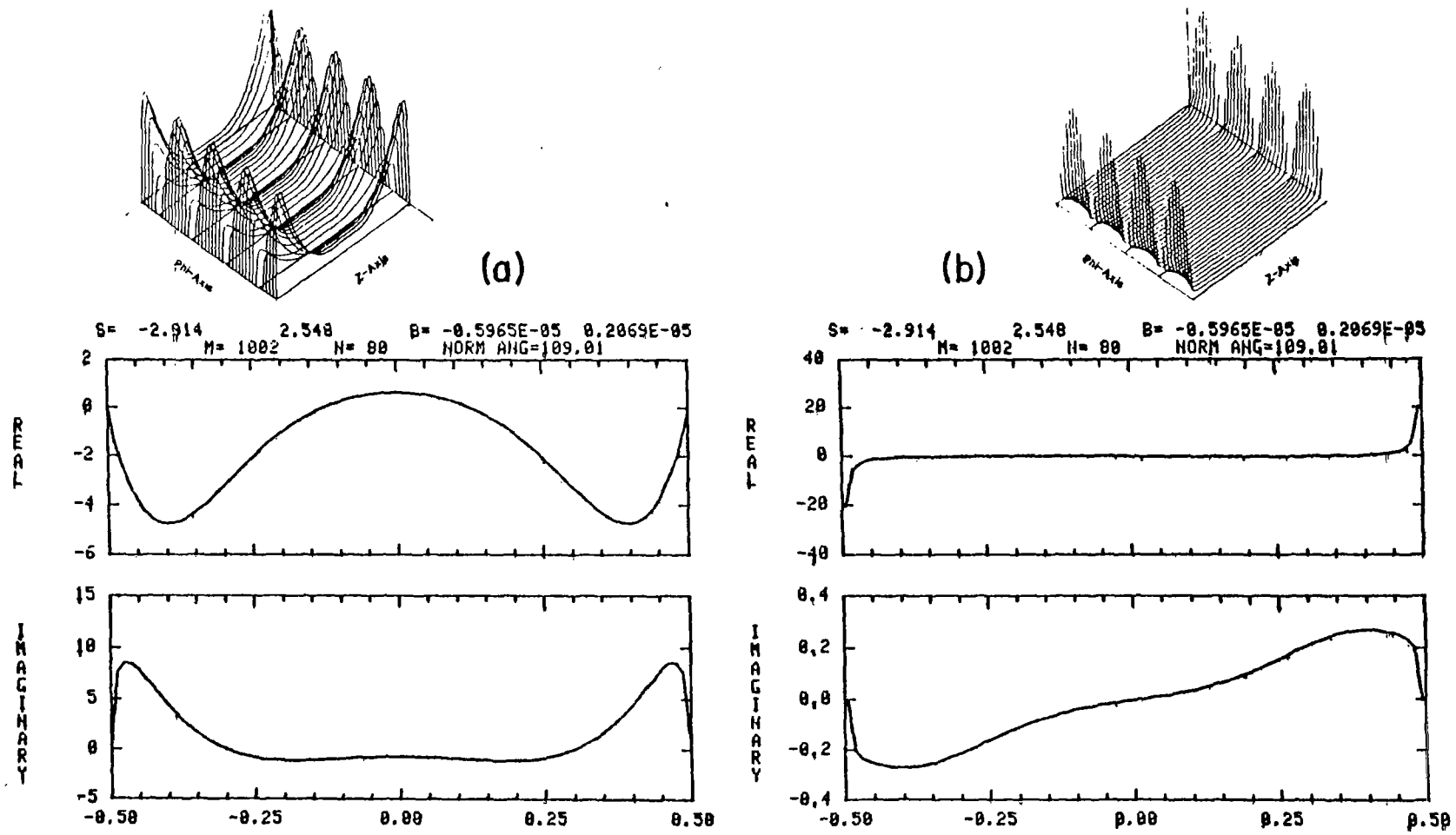

Figure 11. Characterization of the mode associated with the m = 2 harmonic, second pole, and aspect ratio $\alpha = 10$. (a) z-component of current, (b) ϕ-component of current. The z-dependent factor of the modal current is displayed along with a three-dimensional magnitude representation of the dependence on z and ϕ over the unrolled cylinder.

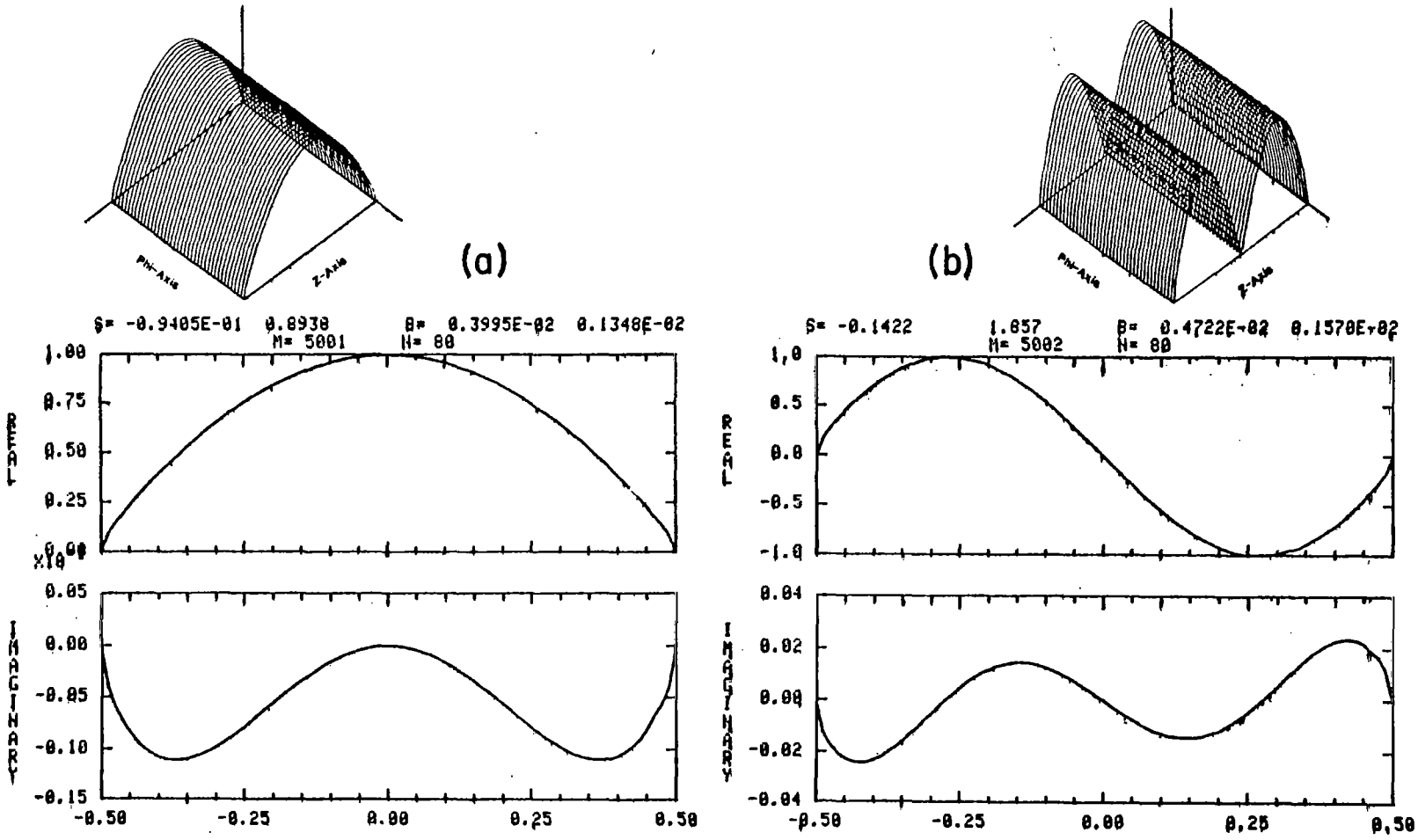

Figure 12. Characterization of the modes associated with the m = 0 harmonic, (a) first pole, (b) second pole, and aspect ratio $\alpha = 50$. The z-dependent factor of the modal current is displayed along with a three-dimensional magnitude representation of the dependence on z and ϕ over the unrolled cylinder.

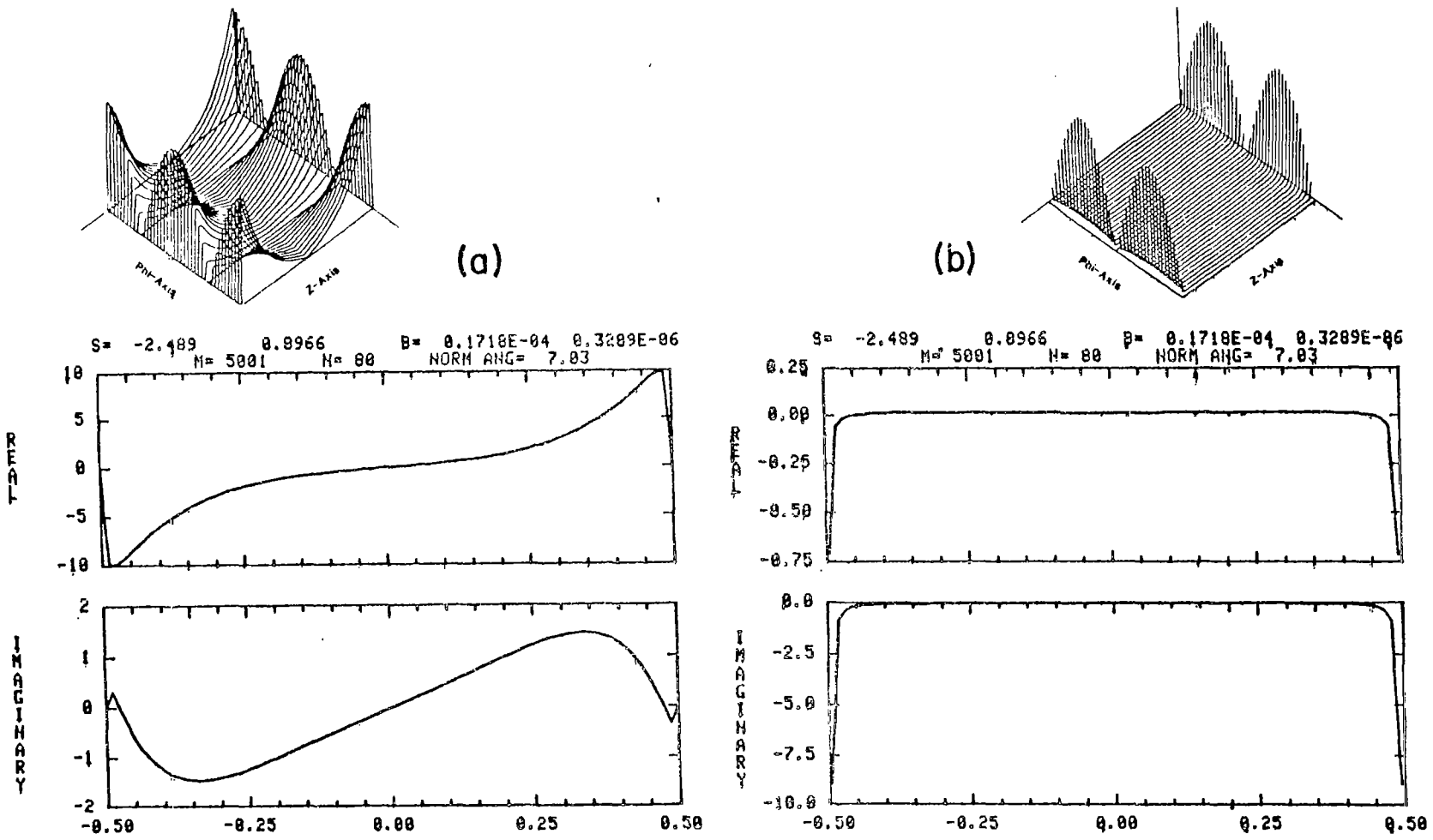

Figure 13. Characterization of the mode associated with the m = 1 harmonic, first pole, and aspect ratio $\alpha = 50$. (a) z-component of current, (b) ϕ-component of current. The z-dependent factor of the modal current is displayed along with a three-dimensional magnitude representation of the dependence on z and ϕ over the unrolled cylinder.

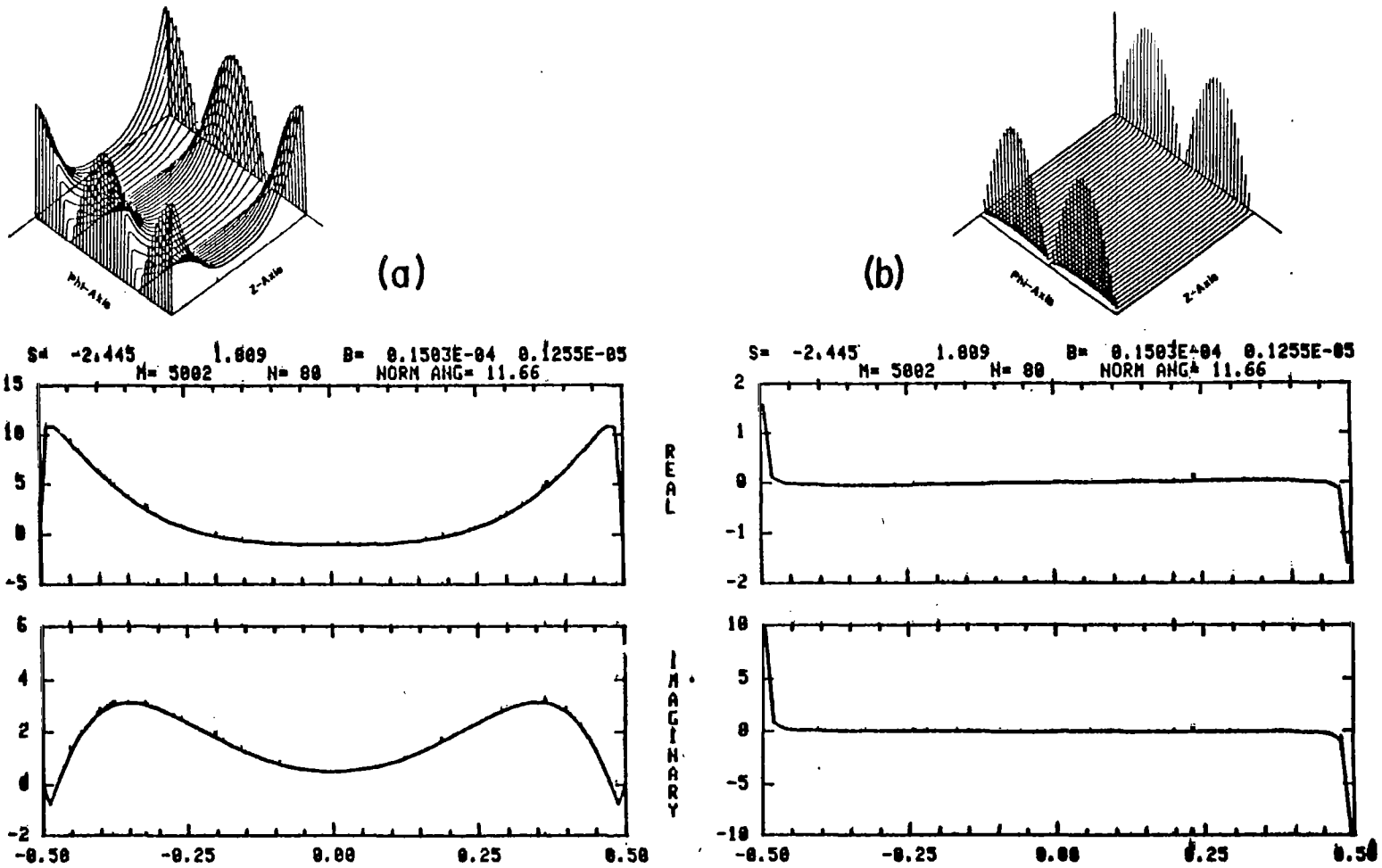

Figure 14. Characterization of the mode associated with the m = 1 harmonic, second pole, and aspect ratio $\alpha = 50$. (a) z-component of current, (b) ϕ-component of current. The z-dependent factor of the modal current is displayed along with a three-dimensional magnitude representation of the dependence on z and ϕ over the unrolled cylinder.

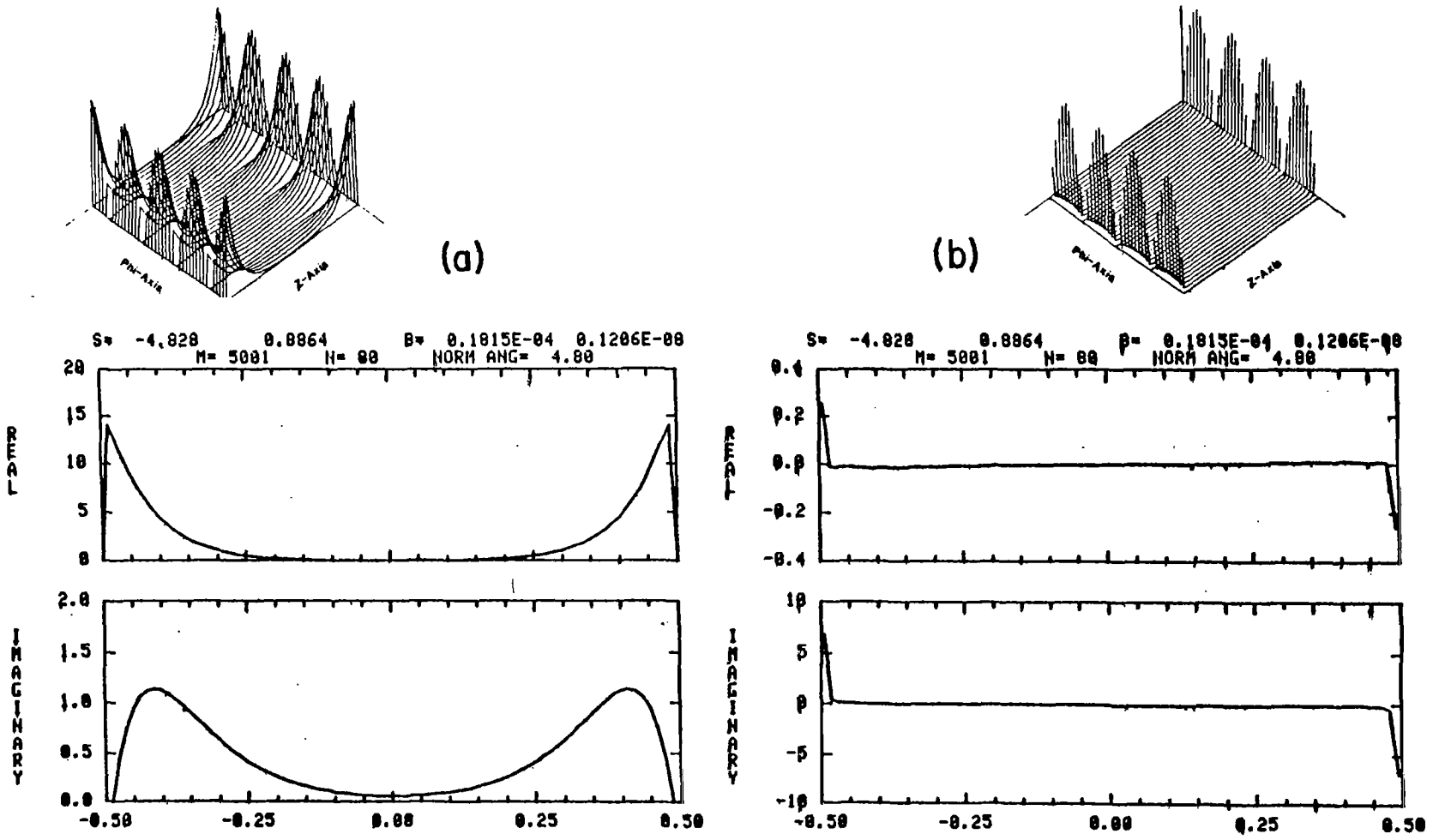

Figure 15. Characterization of the mode associated with the m = 2 harmonic, first pole, and aspect ratio $\alpha = 50$. (a) z-component of current, (b) ϕ-component of current. The z-dependent factor of the modal current is displayed along with a three-dimensional magnitude representation of the dependence on z and ϕ over the unrolled cylinder.

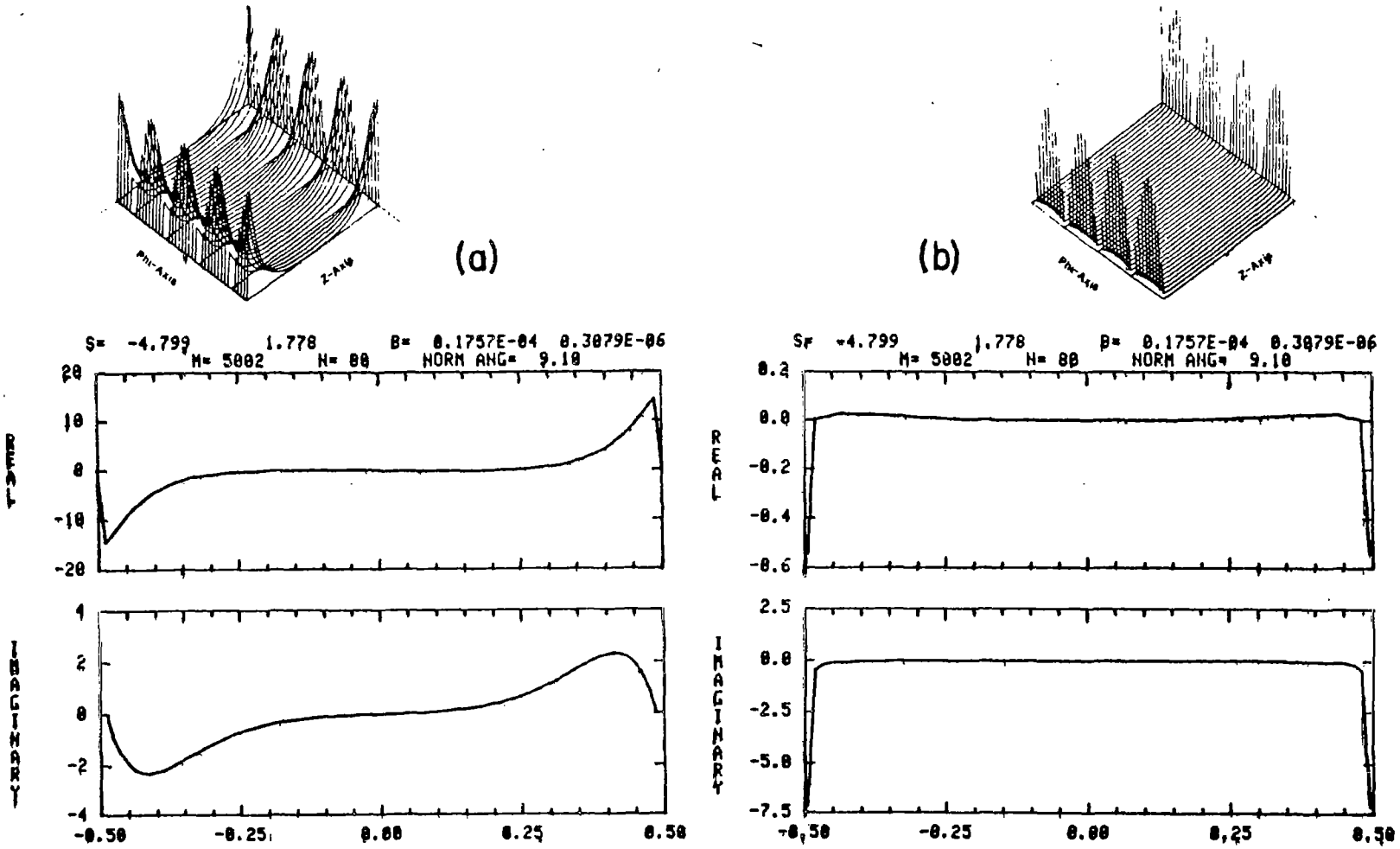

Figure 16. Characterization of the mode associated with the m = 2 harmonic, second pole, and aspect ratio $\alpha = 50$. (a) z-component of current, (b) ϕ-component of current. The z-dependent factor of the modal current is displayed along with a three-dimensional magnitude representation of the dependence on z and ϕ over the unrolled cylinder.

CHAPTER 4

CONCLUSIONS

A selective group of Singularity Expansion Method parameters for an open-ended conducting cylinder are presented in this work. A complete tabulation of the data obtained for this structure can be found in a companion report [9].

A major significance of this work is the insight gained in comparing the features of resonances associated with various order azimuthal current variations. Using the frequency domain SEM description, along with a more complete set of parameters, the resonant behaviour of cylindrical structures due to higher order azimuthal current variations is interpretable. As stated in [6], the major factors in the prediction of aperture coupling are the dominant resonances, i.e., the resonances that lie in closest proximity to the $j\omega$ axis. The torsional effect which produces contradirected pole trajectories of the m=0 poles as opposed to the higher order poles, introduces the possibility of poles associated with higher-order azimuthal modes moving so as to compete with the m=0 poles for dominances. That is, the resonances that lie in closest

proximity to the $j\omega$ axis. The torsional effect discussed in interpreting the pole trajectories of higher azimuthal-order modes poses a possibility which deserves further attention. That is, with m=1 and m=2 pole families moving nearer the $j\omega$ axis as the dominant m=0 family moves out, the poles of these higher-order families begin to "compete" for dominances with the m=0 family thereby presenting a complex dominant pole constellation. It is anticipated that the SEM coupling coefficients will diminish appreciably with increasing mode number thereby diminishing the degree of "competition". This issue should be considered when coupling coefficients are computed.

The physical interpretation in Chapter 3 are preliminary and are likely to prove superficial under closer scrutiny. A detailed study of the phenomena evidenced in the cylinder data may lead to further physical insight into the electromagnetic interaction of a wave with the cylinder. For example, accurately plotting the current streamlines associated with the present data is likely to be helpful. It may be possible to relate the current flow paths over the cylinder with the pole values on a geometrical basis as Howard has done for the sphere [18].

Wilton's conjecture relative to the conversion of interior resonances to radiating resonances can be verified in a more precise fashion if the present numerical model is expanded to incorporate end-caps. By system-

atically opening holes in the end-caps, one can evolve from the closed structure and the associated cavity resonances to the resonances of the open-ended structure considered here.

APPENDIX A

Derivation of the Derivative Term of the Normalization Constant

In the determination of the SEM parameters, a term involving the derivative of the impedance kernel $\bar{\bar{\Gamma}}_m$ with respect to the frequency variable s appears in the normalization constant derivation (2.22a). Viz.

$$\beta_{mi} = \langle \bar{J}_{mi}(\bar{r}'); \partial/\partial s(\bar{\bar{\Gamma}}_m(\bar{r},\bar{r}',s_{mi}); \bar{J}_{mi}(\bar{r}')\rangle^{-1} \qquad (A.1)$$

where $\bar{\bar{\Gamma}}$ is a two-by-two dyadic over the surface of the object identifiable form (2.18):

$$\bar{\bar{\Gamma}}_m(\bar{r},\bar{r}',s) = \begin{bmatrix} \beta_{11m}(\bar{r},\bar{r}',s) & \beta_{12m}(\bar{r},\bar{r}',s) \\ \beta_{21m}(\bar{r},\bar{r}',s) & \beta_{22m}(\bar{r},\bar{r}',s) \end{bmatrix} \qquad (A.2)$$

In the numerical computation of β_{mi}, (A.1) goes over to a matrix counterpart involving the elements of

(2.23) and (2.24). Namely,

$$\beta_{mi} = \{[\bar{I}_{mi}]\ \partial/\partial s[\bar{\bar{Z}}_m(s_{mi})][\bar{J}_{mi}]\}^{-1}, \tag{A.3a}$$

where the moment matrix $[\bar{\bar{Z}}_m]$ is expressable in terms of four terms submatrices which follow from (A.2):

$$\overline{\overline{[Z(s)]}} = \begin{bmatrix} [\beta^{qn}_{11m}(s)] & [\beta^{qn}_{12m}(s)] \\ [\beta^{qn}_{21m}(s)] & [\beta^{qn}_{22m}(s)] \end{bmatrix} \tag{A.3b}$$

Therefore, to compute (A.3a) we need the s-derivatives of each of the four forms appearing as matrix elements in (A.3b), i.e. we need

$$\begin{aligned} \partial/\partial s\ \beta^{qn}_{11m} = \partial/\partial s[(-a/4\pi s\varepsilon\Delta z^2)[&K(z_{n-\frac{1}{2}}, z_{n+\frac{1}{2}}, z_{q+1}, m) \\ &- (2 + (s\Delta z/c)^2)K(z_{n-\frac{1}{2}}, z_{n+\frac{1}{2}}, z_q, m) \\ &+ K(z_{n-\frac{1}{2}}, z_{n+\frac{1}{2}}, z_{q-1}, m)]] \end{aligned} \tag{A.4a}$$

$$\begin{aligned} \partial/\partial s\ \beta^{qn}_{12m} = \partial/\partial s[(-jm/4\pi s\varepsilon\Delta z)[&K(z_{n-\frac{1}{2}}, z_{n+\frac{1}{2}}, z_{q+1}, m) \\ &- K(z_{n-\frac{1}{2}}, z_{n+\frac{1}{2}}, z_q, m)]] \end{aligned} \tag{A.4b}$$

$$\begin{aligned} \partial/\partial s\ \beta^{qn}_{21m} = \partial/\partial s[(-jm/4\pi s\varepsilon\Delta z)[&K(z_{n-\frac{1}{2}}, z_{n+\frac{1}{2}}, z_q, m) \\ &- K(z_{n-\frac{1}{2}}, z_{n+\frac{1}{2}}, z_{q-1}, m)]] \end{aligned} \tag{A.4c}$$

$$\partial/\partial s\ \beta^{qn}_{22m} = \partial/\partial s[(-sa/2c)[K(z_{n-\frac{1}{2}}, z_{n+\frac{1}{2}}, z_q, m+1) + K(z_{n-\frac{1}{2}}, z_{n+\frac{1}{2}}, z_q, m-1)] - (m^2/a)K(z_{n-\frac{1}{2}}, z_{n+\frac{1}{2}}, z_q, m)] \quad \text{(A.4d)}$$

with

$$K(z_1, z_2, z_q, m) = \int_{z_1}^{z_2} G_m(z_q, z')\ dz' \quad \text{(A.5)}$$

and the natural resonances will be normalized to

$$cz = sL/c\pi \quad \text{(A.6)}$$

where c is the velocity of light and L is normalized to 1. Substituting (A.6) into (A.5), and differentiating with respect to s, we obtain

$$\partial/\partial s(K(z_1, z_2, z_q, m)) = \int_{z_1}^{z_2} \partial/\partial s(G_m(z_q, z')\ dz'$$

$$= \int_{z_1}^{z_2} \int_{-\pi}^{\pi} \partial/\partial s(\exp(-cz\pi R)\ \cos(m\xi)\ d\xi dz'$$

$$= \int_{z_1}^{z_2} \int_{-\pi}^{\pi} (-1/c)\ \exp(-cz\pi R)\ \cos(m\xi)\ d\xi dz'$$

$$= (-1/c) \int_{z_1}^{z_2} g_m(z_q, z')\ dz'$$

where

$$g_m(z_q,z') = \int_{-\pi}^{\pi} \exp(-cz\pi R)\cos(m\xi)\, d\xi \,. \qquad (A.7)$$

Therefore

$$\partial/\partial s(K(z_1,z_2,z_q,m)) = (-1/c)k(z_1,z_2,z_q,m) \qquad (A.8)$$

where

$$k(z_1,z_2,z_q,m) = \int_{z_1}^{z_2} g_m(z_q,z')\, dz' \qquad (A.9)$$

Substituting (A.6) into (A.4), where $K(z_1,z_2,z_q,m)$ has been abbreviated by $K_m(z_q)$

$$\partial/\partial s(\beta_{11m}^{qn}) = -30ac/\Delta z^2[\partial/\partial s(K_m(z_{q+1})/s) - \partial/\partial s((2 + (s\Delta z/c)^2)K_m(z_q)/s) + \partial/\partial s(K_m(z_{q-1})/s)] \qquad (A.10a)$$

$$\partial/\partial s(\beta_{12m}^{qn}) = -j30mc/\Delta z[\partial/\partial s(K_m(z_{q+1})/s) - \partial/\partial s(K_m(z_q)/s)] \qquad (A.10b)$$

$$\partial/\partial s(\beta_{21m}^{qn}) = -j30mc/\Delta z[\partial/\partial s(K_m(z_q)/s) - \partial/\partial s(K_m(z_{q-1})/s)] \qquad (A.10c)$$

$$\partial/\partial s(\beta_{22m}^{qn}) = 15a/c[\partial/\partial s(sK_{m+1}(z_q)) + \partial/\partial s(sK_{m-1}(z_q))] + 30m^2c/a[\partial/\partial s(K_m(z_q)/s)] \qquad (A.10d)$$

We may carry out the differentiation on the terms of the form

$K(z)/s$

to obtain

$$\partial/\partial s(K(z)/s) = [(-s/c)k(z) - K(z)]/s^2 . \qquad \text{(A.11a)}$$

Differentiating terms of the form

$sK(z)$

yields

$$\partial/\partial s(sK(z)) = [K(z) - (s/c)k(z)] . \qquad \text{(A.11b)}$$

Expanding the terms in (A.10) containing derivatives, using the forms obtained in (A.11), produces

$$\begin{aligned}\partial/\partial s(\beta_{11m}^{qn}) = -30ac/\Delta z^2[&-k_m(z_{q+1})/sc + 2k_m(z_q)/sc + (s\Delta z^2/c^3)k_m(z_q) \\ &- k_m(z_{q-1})/sc - K_m(z_{q+1})/s^2 - 2K_m(z_q)/s^2 \\ &+ (s\Delta z^2/c^2)K_m(z_q) - K_m(z_{q-1})/s^2]\end{aligned} \qquad \text{(A.12a)}$$

$$\begin{aligned}\partial/\partial s(\beta_{12m}^{qn}) = -j30mc/\Delta z[&-k_m(z_{q+1})/sc + k_m(z_q)/sc \\ &- K_m(z_{q+1})/s^2 + K_m(z_q)/s^2]\end{aligned} \qquad \text{(A.12b)}$$

$$\partial/\partial s(\beta_{21m}^{qn}) = -j30mc/\Delta z[-k_m(z_q)/sc + k_m(z_{q-1})/sc$$

$$-K_m(z_q)/s^2 + K_m(z_{q-1})/s^2]$$

(A.12c)

$$\partial/\partial s(\beta_{22m}^{qn}) = 15a/c[-sk_{m+1}(z_q)/c - sk_{m-1}(z_q)/c + K_{m+1}(z_q)$$

$$+ K_{m-1}(z_q)] + 30m^2c/a[-k_m(z_q)/sc - K_m(z_q)/s^2] .$$

(A.12d)

Rearranging (A.12) and using the normalized pole term

$cz = sL/c\pi$

where L is normalized to 1 and c is the velocity of light, then

$$\partial/\partial s(\beta_{11m}^{qn}(J_z)) = -30a/(cz)\pi\Delta z^2[(-1/c)[k_m(z_{q+1})$$

$$- (2 + ((cz)\pi\Delta z)^2)k_m(z_q) + k_m(z_{q-1})]$$

$$- (1/(cz)\pi c)[K_m(z_{q+1}) - (2 - ((cz)\pi\Delta z)^2)K_m(z_q)$$

$$+ K_m(z_{q-1})]]$$

(A.13a)

$$\partial/\partial s(\beta_{12m}^{qn}(J_\phi)) = -j30m/\Delta z(cz)\pi[(-1/c)[k_m(z_{q+1}) - k_m(z_q)]$$

$$- (1/(cz)\pi c)[K_m(z_{q+1}) - K_m(z_q)]]$$

(A.13b)

$$\partial/\partial s(\beta^{qn}_{21m}(J_z)) = -j30m/\Delta z(cz)\pi[(-1/c)[k_m(z_q) - k_m(z_{q-1})]$$

$$- (1/(cz)\pi c)[K_m(z_q) - K_m(z_{q-1})]] \qquad \text{(A.13c)}$$

$$\partial/\partial s(\beta^{qn}_{22m}(J_\phi)) = 15a/c[K_{m+1}(z_q) + K_{m-1}(z_q)] - 30m^2/a(cz)^2\pi^2 c[K_m(z_q)]$$

$$- 15a(cz)\pi/c[k_{m+1}(z_q) + k_{m-1}(z_q)]$$

$$- 30m^2/a(cz)\pi c[k_m(z_q)]. \qquad \text{(A.13d)}$$

Upon careful examination of eq.(A.13), it can be observed that except for eq.(A.13a), the terms involving the K integrals are the same integral terms used in the determination of the pole values. Therefore, if managed carefully, the terms above can be calculated very efficiently, since part of the integrals have already been evaluated, and can be reused. The only remaining integral terms are non-singular.

APPENDIX B

Singularity Analysis for the Self Term of the Body of Revolution Formulation

Upon calculation of the impedance matrix for the body of revolution, one encounters a singularity in the integrand of the integral function K, when the field point is within the source region. The numerical treatment of this singularity is presented in this appendix. This formulation follows, in part, from Glisson and Wilton's treatment of the singularity [8], but uses the elliptic integral treatment of Pearson [15].

For a self term of the moment matrix, the K integral function of (2.42) may be written as

$$K = \int_{z_1}^{z_2} \int_{-\pi}^{\pi} (\exp(-sR_0/c)/R_0)\cos(m\xi)\, d\xi dz' \qquad (B.1a)$$

where

$$R_0 = [(\rho - \rho')^2 + 2\rho\rho'(1-\cos m\xi) + (z-z')^2]^{\frac{1}{2}} \qquad (B.1b)$$

As $\rho \to \rho'$, $z \to z'$, and $\xi \to 0$, then $R \to 0$ and the integrand of

(B.1a) is singular. K can be expressed as

$$K = I_1 + I_2 \tag{B.2}$$

where I_1 and I_2 are defined as

$$I_1 = \int_{z_1}^{z_2} \int_{-\pi}^{\pi} ((\exp(-sR_0/c))\cos(m\xi) - 1)/R_0 \, d\xi dz' \tag{B.3a}$$

$$I_2 = \int_{z_1}^{z_2} \int_{-\pi}^{\pi} 1/R_0 \, d\xi dz' \tag{B.3b}$$

where the integrand of (B.3a) is no longer singular.

Rewriting Ro as

$$R_0 = [(\rho - \rho')^2 + (z - z')^2 + 4\rho\rho' \sin^2(\xi/2)]^{1/2}$$

$$= R_1[1 + \beta_1^2 \sin^2(\xi/2)]^{1/2}$$

with

$$R_1 = [(\rho - \rho')^2 + (z - z')^2]^{1/2}$$

and

$$\beta_1 = Z[\rho\rho']^{1/2}/R_1.$$

Thus with a simple change of variable, I_2 may be written as [16]

$$I_2 = 4 \int_{z_1}^{z_2} \int_0^{\pi/2} 1/R_1 [1 + \beta_1^2 \sin\zeta]^{\frac{1}{2}} \, d\zeta dz'$$

$$= 4 \int_{z_1}^{z_2} (1/R_1 [1 + \beta_1^2]^{\frac{1}{2}}) K^e [\beta_1/(1 + \beta_1^2)^{\frac{1}{2}}] \, dz'$$

$$= 4 \int_{z_1}^{z_2} K^e(\beta_2)/R_2 \, dz' \qquad (B.4)$$

where $K^e(\beta)$ is a complete elliptic integral of the first kind, defined by

$$K^e(\beta) = \int_0^{\pi/2} 1/(1 - \beta^2 \sin^2\phi)^{\frac{1}{2}} \, d\phi \qquad (B.5)$$

and

$$R_2 = [(\rho + \rho')^2 + (z - z')^2]^{\frac{1}{2}}$$

$$\beta_2 = 2[\rho\rho']^{\frac{1}{2}}/R_2.$$

The integrand of (B.4) is still singular. It is at this point that the formulation presented here differs from

Wilton and Glisson's formulation. This logarithmic singularity is handled as presented by Pearson [15]. Namely,

$$\int_{z_1}^{z_2}\int_{-\pi}^{\pi} (\exp(-sR_0/c)\cos(m\xi))/R_0 \, d\xi dz' = -2/a[(z_2 - z_1)$$

$$- (z_2 - z)\ln(z_2 - z) - (z - z_1)\ln(z - z_1)]$$

$$+ \int_{z_1}^{z_2}\int_{-\pi}^{\pi} (\exp(-sR_0/c)\cos(m\xi) - 1)/R_0 \, d\xi dz'$$

$$+ \int_{z_1}^{z_2} (2(1-\beta)/a)\ln|z - z'| \, dz' + \int_{z_1}^{z_2} (2\beta/a)[\ln 8a - \ln\beta$$

$$+ (1/2)^2[\ln(4/\beta') - 2/(1\cdot 2)]\beta'^2 + (1\cdot 3/2\cdot 4)^2[\ln(4/\beta') - 2/1\cdot 2$$

$$- 2/3\cdot 4]\beta'^6 + \cdots] \, dz' \qquad (B.6)$$

where

$$\beta = 2[\rho\rho']^{1/2}/R_2 = 2a/R_2$$

and

$$\beta' = [1 - \beta^2]^{1/2}.$$

Equation (B.6) is used only in the determination of the singular integrals for the self zones.

Following the convention suggested by Wilton and Glisson in [8], the non-self term integrals will be evaluated by separating the integrand into two parts. The non-self zone integrals are evaluated combining eq.(B.3a) and (B.4). Therefore, for non-self zones, K is evaluated by

$$K = \int_{z_1}^{z_2} \int_{-\pi}^{\pi} \exp(-sR_0/c)\cos(m\xi)/R_0 \, d\xi dz'$$

$$= \int_{z_1}^{z_2} \int_{-\pi}^{\pi} (\exp(-sR_0/c)\cos m\xi - 1)/R_0 \, d\xi dz' + 4 \int_{z_1}^{z_2} K^e(\beta_2)/R_2 \, dz' . \tag{B.7}$$

APPENDIX C

Normalizations

All poles presented in this work have been normalized to $L/c\pi$. However, the natural modes and the normalization constants for the m=0, and higher order azimuthal variation cases have been normalized differently.

The natural modes presented for the m=0 case have been normalized on a peak magnitude basis in order to compare with Tesche [4]. The natural modes presented for the higher order modes have been normalized to the norm presented in (2.33). The norm calculated in (2.33) is a complex quantity. Thus, the natural modes have been normalized to the magnitude and the associated angle is presented as NORM ANG on each graph.

The normalization constant presented for the m=0 case and higher order cases have been normalized to L/c. However, for comparision with Tesche [4], the current natural modes associated with the higher order azimuthal variation were converted to total current modes, rather than current density modes, which were calculated using the preceding formulation. The total current natural modes are $2\pi a$ times the current density natural modes,

where a is the radius of the cylinder. Therefore, for the m=0 case, the normalization constants are associated with the total current rather than with current density natural modes.

REFERENCES

1. Baum, C. E., "On the Singularity Expansion Method for the Solution of Electromagnetic Interaction Problems," Interaction Note 88, December 11, 1971.

2. Baum, C. E., "The Singularity Expansion Method," in L. B. Felson, ed., Transient Electromagnetic Fields, Springer-Verlog, Berlin-Heidelberg-New York, 1976.

3. Baum, C. E., "Toward an Engineering Theory of Electromagnetic Scattering: The Singularity and Eigenmode Expansion Methods," in P. L. E. Ushlengthi, ed., Electromagnetic Scattering, Academic Press, New York-San Francisco-London, 1978.

4. Tesche, F. M., "The Far-Field Response of a Step-Excited Linear Antenna Using SEM," IEEE Trans. Antenna Propagat., Vol. AP-23, pp. 834-838, November, 1975; also Sensor and Simulation Note 177, The Dikewood Corporation, Albuquerque, New Mexico, May, 1973.

5. Pearson, L. W., "Applications of the Singularity Expansion Method," in Short Course Notes; Numerical and Asymptotic Techniques for Electromagnetics and Antennas, Blue Mountain Lake, New York, 1979; also University of Kentucky Electromagnetics Research Report, October, 1979.

6. Pearson, L. W., "Phenomenological Interpretation of the Penetration of Electromagnetic Energy into Finite-Extent Closed Shells," University of Kentucky Electromagnetics Research Report, In preparation.

7. Mautz, J. R. and R. F. Harrington, "Radiation and Scattering From Bodies of Revolution," Appl. Sci. Res., Vol. 20, pp. 405-435, June, 1969.

8. Glisson, A. W. and D. R. Wilton, "Simple and Efficient Numerical Techniques for Treating Bodies of Revolution," Technical Report for RADC Contract No. F30602-78-C-0120, University of Mississippi, University, Mississipppi, March 1979.

9. Melson, G. B. and L. W. Pearson, "SEM Characterization of an Open-Ended Cylinder," University of Kentucky Electromagnetics Research Report, November, 1980.

10. Harrington, R. F., Field Computation by Moment Methods, The MacMillan Company, New York, 1968.

11. Tesche, F. M., "On the Singularity Expansion Method as Applied to Electromagnetic Scattering From Thin Wires," Interaction Notes, Note 102, April, 1972.

12. Singaraju, B. K., D. V. Giri and C. E. Baum, "Further Developments in the Application of Contour Integration to the Evaluation of the Zeros of Analytic Functions and Relevant Computer Programs," Mathematics Note 42, Air Force Weapons Laboratory, Albuquerque, New Mexico, March, 1976.

13. Wilton, D. A., A. W. Glisson and C. M. Butler, "Numerical Solutions for Scattering by by Rectangular Bent Plane Structures," Final Report, Contract No. N00123-75-C-1372 for Naval Electronics Laboratory Center (now Naval Ocean System Center), University of Mississippi, University, Mississippi, October 1976.

14. Umashankar, K. R. and D. R. Wilton, "Transient Characterization of Circular Loop Using Singularity Expansion Method," Interaction Note 259, University of Mississipppi, University, Mississippi, August, 1974.

15. Pearson, L. W., "A Separation of the Logarithmic Singularity in the Exact Kernel of the Cylindrical Antenna Integral Equation," IEEE Trans. Antennas Propagat., Vol. AP-23, No. 2, pp. 256-258, March, 1975.

16. Gradshteyn, I. S. and I. M. Ryzhik, Tables of Integrals, Series, and Products. Academic Press, New York, p. 173, 1965.

17. Wilton, D. R. and A. W. Glisson, "Implications of Antenna and Scatterer Topology for SEM Terms," Mini-Symposium on Electromagnetic Topology; University of New Mexico, Albuquerque, New Mexico, March, 1980.

18. Howard, A. Q., "A Geometric Theory of Natural Oscillation Frequencies in Exterior Scattering Problems," Interaction Note 378, Department of Electrical Engineering, University of Arizona, October, 1979.